

Improved optical transitions theory for superlattices and periodic systems; new selection rules

Pedro Pereyra

*Física Teórica y Materia Condensada, UAM-Azcapotzalco,
Av. S. Pablo 180, C.P. 02200, México D. F., México*

(Dated: September 19, 2016)

Using the genuine superlattice eigenvalues and eigenfunctions, and the eigenfunctions parity symmetries, discussed recently, new optical-transition selection rules are derived, and a novel and basically different theoretical approach for explicit calculation of optical responses of light-emitting periodic structures is presented here. To show the scope of this approach, we review and revisit a number of photoluminescence and infrared measurements reported in the literature. The photoluminescence and infrared spectra of superlattices based on (Al,Ga)As and (In,Ga)N, with clear spectrum features, high resolution and different superlattice characteristics, comprising small (~ 10) and large (~ 400) number of unit-cells, wide and narrow barrier and valley widths, varying from 2.5nm to ~ 40 nm, have been recalculated. The plots obtained here for the optical response of the chosen systems, reproduce rather well the observed photoluminescence or infrared spectra. We show that the narrow peaks clustered in groups that were observed in blue-emitting superlattices, but couldn't be explained before, are faithfully reproduced and fully understood. We show that this replication of groups of peaks and the isolated peak observed in high resolution spectra, are interesting effects neatly determined by the recently unveiled tunable surface-energy-levels detachment. Among the various properties and differences discussed in the paper, we find significant that the observed optical transitions, forbidden before, are now allowed and accounted. Since the number of allowed matrix-elements, $\sim n^2 n_c n_v / 2$, can be extremely large when the number of unit cells, n , and the number of subbands in the conduction and valence bands, n_c and n_v , are large, we devote the last part of this paper to reduce this number and to show that, essentially, the same spectra is obtained when, besides the symmetry selection rules, other leading order selection rules, closely related to intra-subband symmetry, are introduced. These rules reduce the number of matrix-elements evaluations from $\sim n^2 n_c n_v / 2$ to $\sim n n_c n_v / 2$, i.e., depending on the SL, from about 1000 to 100. We comment also on a third rule, that picks up the contributions of the surface and edge states, and show that it reduces further the number of transitions to $N_s \leq n_c n_v$. With these rules, the main peaks are conserved and their number practically matches with that of the actual spectrum. Excellent agreements with experimental results are found.

PACS numbers: 03.65.Ge, 42.50.-p, 42.50.Ct, 68.65.Ac, 73.20.-r, 78.30.Fs, 78.55.Ap, 78.66.Fd, 78.67.Pt, 85.60.-q

I. INTRODUCTION

Despite the broad theoretical and empirical knowledge of the light-matter interactions¹ and the overwhelming variety of device applications, the actual quantum mechanical description of photoemission and photoabsorption processes involving periodic semiconductor structures, suffer from important limitations. The main problem in the theoretical calculations, using the golden rule

$$|\langle \psi_f | H_{\text{int}} | \psi_i \rangle|^2 / [E_f - E_i + \hbar\omega]^2 + \Gamma_i^2], \quad (1)$$

has been the lack of explicit knowledge of the initial and final states, $|\psi_i\rangle$ and $|\psi_f\rangle$, and of the corresponding energies, E_i and E_f . In the standard approach to periodic systems, the energy levels become bands or subbands, and the initial and final superlattice (SL) states, written in terms of Bloch functions,² are generally unknown.³ However, in the alternative theory of finite periodic systems, the identifiable energy levels are recovered and the quantum states of semiconductor heterostructures, like quantum wells and superlattices, are explicitly known.⁴ Our purpose here is to present an improved optical

transitions theory for periodic systems, based on *bona fide* eigenfunctions and their parity symmetries recently unravelled.⁶

To understand better the scope and the need of an alternative approach to calculate the optical response, let as briefly outline, in this introduction, the essential features, limitations and advantages of the standard and the new approach for the calculation of the physical quantities relevant to the light emission processes.

Soon after the introduction of semiconductor superlattices,^{7,8} the miniband structures of direct and indirect band gap semiconductors were experimentally and theoretically confirmed,⁹⁻²⁵ and the optical properties of superlattices became overwhelmingly studied.²⁶⁻³⁵ Concerning the theoretical approaches applied to study these systems, Leo Esaki noticed that whereas in reality the SLs contain a finite number of layers, with a finite number of atomic cells each, the standard theoretical approaches tacitly assume that the SLs are infinite-periodic structures with alternating layers containing also an infinite number of atomic cells.³⁶ In fact, the wave functions are generally written as $\psi(\mathbf{r}) = \sum_l u_{nl}(\mathbf{r}) f_l(\mathbf{r})$, with $u_{nl}(\mathbf{r})$ the periodic part

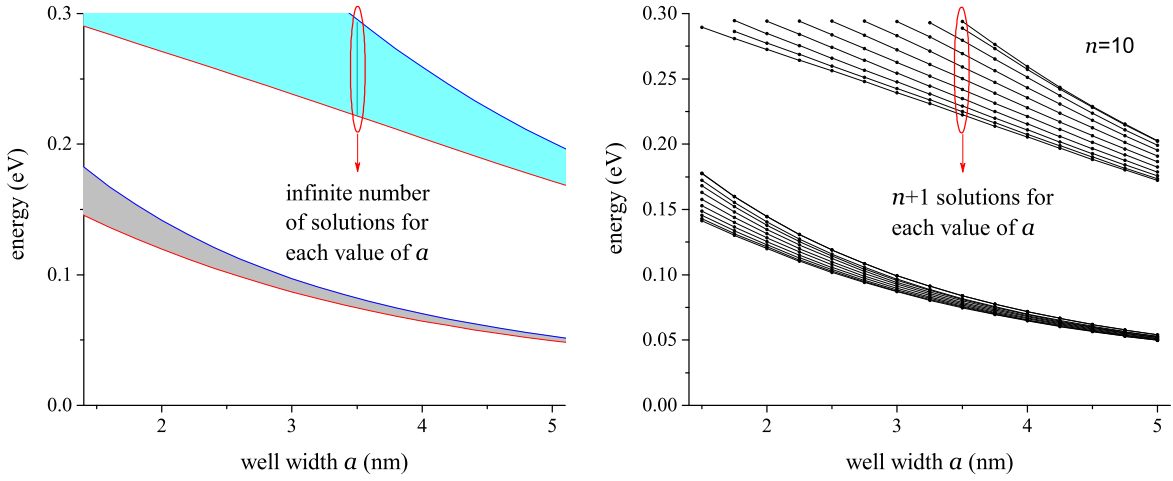


FIG. 1. Continuous and discrete first two subbands of the conduction band, as functions of the well width a , obtained for a Kronig-Penney-like periodic potential in the standard approach (left) and in the TFPS (right).

of the host-semiconductor Bloch's function at band n_l , and $f_l(\mathbf{r}) \propto \exp[i\mathbf{k}_\perp \cdot \mathbf{r}_\perp] \chi_l(z)$ the envelope wave function. For SLs this is, again, written in terms of Bloch-type functions $\chi_\mu(z) = \exp(iqz)u_\mu(z)$, characterized by a subband index μ and a continuous wave number q that is then artificially discretized, via the cyclic boundary condition. But, as Bastard states in Ref. [3], "...the Bloch functions are seldom known explicitly ...". Thus, no explicit calculation of matrix elements $\langle \psi_f | H_{\text{int}} | \psi_i \rangle$ involving subbands is known. The explicit matrix elements are replaced by the so-called oscillator strengths f_{fi} , statistical assumptions and sum rules.

When the calculation of optical matrix-elements is pursued in the standard approaches,^{20,31,37} the calculation ends up evaluating at the center of the Brillouin zone or at the subband edge,^{37,38} $q = 0$. With continuous subband structures obtained from Kronig-Penney theory, and the single-quantum-well eigenfunctions as envelope function with the ensuing selection rule $\Delta\mu = \mu - \mu' = 0$, widely used to explain the optical transitions structure.^{31,48} Luo et al.²⁰ suggested also $\Delta\mu = 0, \pm 1$ for narrow gap materials. The limits of this approach became apparent when optical transitions, "forbidden" by these rules, were observed,^{45,49–53} and when important features of photoluminescence spectra, obtained in high-resolution measurements, could not be explained.^{54–56} It is worth noticing that, independent of the models' limitations to solve the Schrödinger equation for periodic potentials, the effective-mass^{39–41} and the envelope-function^{5,42,43} approximations are important advances in the aim to work out the quantum problem of heterostructures and SLs.^{3,5,20,37,44–47}

On the other side, the theory of finite periodic systems (TFPS) grew up along the last 50 years, in the spirit of the Landauer's scattering approach,⁶² and the electromagnetic theory of periodic media.^{63,64} Transport properties of periodic semiconductor systems, modelled

as Kronig-Penney like⁶⁵ square barriers and wells in the effective mass approximation, have been studied.^{4,66–87} This approach evolved and the TFPS has been generalized to include periodic structures with arbitrary potential profiles, arbitrary number n of unit cells and arbitrary number \mathcal{N} of propagating modes for open, bounded and quasi-bounded SLs.^{4,79,81–84} As was amply explained in these references, important physical quantities, like the eigenvalues, eigenfunctions and transmission coefficients, are straightforwardly obtained without recurring to Bloch's theorem, but using simple algebraic procedures and general transfer-matrix properties, i.e., with the same elementary mathematics that we use to solve quantum-mechanics textbook examples.⁸⁸ The theory, is based on the transfer matrix method, and the important combination property that makes possible to express the n -cells transfer matrix M_n as M^n , where M is the single-cell transfer matrix. This relation, $M_n = M^n$, has been rigorously transformed into the non-commutative recurrence relation

$$p_n - (\beta^{-1}\alpha\beta + \alpha^*)p_{n-1} + p_{n-2} = 0. \quad (2)$$

and solved.⁷⁹ The matrix polynomials p_n of dimension $\mathcal{N} \times \mathcal{N}$ become, in the one-propagating mode approximation, the Chebyshev polynomials of the second kind U_n . Given these polynomials, the transfer-matrix blocks $M_n(i, j)$, for time reversal invariant systems, are: $M_n(1, 1) = \alpha_n = p_n - \alpha^* p_{n-1} = M_n^*(2, 2)$ and $M_n(1, 2) = \beta_n = \beta p_{n-1} = M_n^*(2, 1)$, with α and β the single cell transfer matrix elements. The matrix M_n and the polynomials p_n carry, like the scattering matrix, the whole information of the physical processes in the system, and depend explicitly on the system size, i.e. on n . Analytical expressions for important physical quantities, like the scattering amplitudes, t_n and r_n , the eigenfunctions $\phi_{\mu\nu}(z)$ and the eigenvalues $E_{\mu\nu}$, have been obtained.

It is worth to stress here that, whereas in the infinite-

periodic approaches to SLs,^{3,12,20,37,48,58–61} each subband (with an infinite number of energy levels, see figure 1) is described by a function $\chi_\mu(z)$ characterized by a single index μ , in the theory of finite periodic systems the subbands (for a system with an arbitrary number of unit cells n) are completely resolved and each subband μ is characterized by a finite set of explicitly determined eigenfunctions $\phi_{\mu\nu}(z)$ and eigenvalues $E_{\mu\nu}$, where the index ν labels the intra-subband levels with values $\nu=1, 2, \dots, n+1$.^{4,79} Each eigenfunction $\phi_{\mu\nu}(z)$, as shown in Ref. [6], has a well defined parity determined by the subband index μ , the intra-subband index ν and the number of unit cells n . It is clear, because of this difference, that not only the transition matrix elements but also the selection rules will not coincide.

Since the TFPS is, clearly, the appropriate approach to study superlattices, and the theoretical descriptions of the optical response has been surpassed by the experimental developments, we present here a detailed discussion and explicit calculations of optical responses using this approach. We will discuss the optical-response-calculation problem in general and we will also apply to specific systems.

Before we focus on the optical-response calculation problem, let us highlight some issues and results that will be faced in this approach. From experimental measurements and theoretical calculations,^{13,31,54–57,85,89} that the subband-separations and subband-widths in SLs are of the order of one tenth of the band offsets, with intra-subband level separations of the order of 1 meV. Real transitions occur between discrete states in the subbands. We will see that given a SL, one can perfectly distinguish energy eigenvalues that differ by 10^{-10} eV or less. This will allow us to describe high accuracy photoluminescence (PL) spectra, with peak separations of the order of 1 meV or less, that were identified as longitudinal modes.^{26,54}

An important problem that comes out when the subband structure is resolved, is the large number of matrix elements that one has, in principle, to evaluate. For a SL with n unit cells, n_c subbands in the conduction band and n_v subbands in the valence band, the number of energy levels (hence of eigenfunctions), for energies below the barrier-heights, is $(n+1)(n_c+n_v)$ and the number of optical transitions is $N=(n+1)^2 n_c n_v$. This means that for a SL of length $L \simeq 1\mu$ and unit-cells length $l_c \sim 50\text{nm}$, like in Ref. [31], the number of possible transitions, for $n_c=3$ and $n_v=4$, is $N \sim 5,000$. This is a large number. One of the purposes of this paper is to reduce substantially this number based on new selection rules based on important symmetries. We will show that using the eigenfunctions symmetries, derived in Ref. [6], we will establish the symmetry selection rules that will reduce the number of matrix-elements evaluations to $N/2$. We will then discuss a couple of rules. The leading order selection rule determined by the subbands symmetry and the edge states rules, which reduce substantially the number of optical transitions into one of the order of $n_c n_v \sim 10$,

giving essentially the same photoluminescence (PL) and infrared (IR) results. We will apply these rules for a number of specific examples.

In the second section, we will outline the theoretical model for optical response of SLs and the eigenfunctions parity symmetry relations found in Ref. [6]. In the third section, after writing the selection rules based on the eigenfunction parity symmetries, we will consider three illustrative examples. We choose as the first examples two of the Nakamura's high precision PL spectra for the blue emitting $\text{GaInN}\backslash(\text{In}_x\text{Ga}_{1-x}\text{N}\backslash\text{In}_y\text{Ga}_{1-y}\text{N})^n\backslash\text{Al}_{0.2}\text{Ga}_{0.8}\text{N}$ SLs, for $n=10$ and for $n=7$. We will show that the observed resonant spectrum and group structure, that couldn't be explained before, will be fully explained. We will show in the second case the effect of the cladding-layers asymmetry. We will then consider the IR spectra of the $(\text{Al}_{0.3}\text{Ga}_{0.7}\text{As}\backslash\text{GaAs})^n$ SLs studied by Helm et al., where the number of unit cells n is of the order of 400. We will discuss the effect of n and show that equivalent results can be obtained when the number of unit cells is, say, of the order of 20. We conclude section III with a brief discussion on the characteristic resonance line-shapes, as well as the exciton binding energies effects on the PL spectra. As a specific example, we will consider one of the various results reported by Masselink et al. for $(\text{Al}_{0.3}\text{Ga}_{0.7}\text{As}\backslash\text{GaAs})^n$ SLs.

In section IV, we discuss the leading order rules. We will conclude the paper with a brief discussion, in section V on the surface and edge-states rules (SESR), implying a minimum of matrix-elements evaluations, of the order of $n_c n_v$, with essentially the same results as with $N/2$ matrix evaluations. In the appendix we will extend the Leavitt-Little model to include the exciton binding energy in the first excited state.

II. THE SLS OPTICAL RESPONSE IN THE TFPS

To study the optical transitions in a superlattice, in the presence of an electromagnetic (EM) field, we consider the Hamiltonian

$$H = H_o + H_{EM} + H_I, \quad (3)$$

where⁹⁰

$$H_o = -\frac{\hbar^2}{2m_e^*} \nabla_e^2 + V_e(z_e) + \frac{\hbar^2}{2m_h^*} \nabla_h^2 + V_h(z_h) + V_{eh}(|\mathbf{r}_e - \mathbf{r}_h|) \quad z_L \leq z_e, z_h \leq z_R \quad (4)$$

describes an (*electron-hole*) pair in the finite periodic potentials $V_e(z_e)$ and $V_h(z_h)$, being V_{eh} the Coulomb interaction potential. H_{EM} describes the transverse EM field and H_I the exciton-field interaction. In this approach, the main part of the quantum problem is centered in solving the electron and hole SL Schrödinger equations

$$\left(-\frac{\hbar^2}{2m_e^*} \nabla_e^2 + V_e(z_e) \right) \varphi_{\mu,\nu}(z_e) = E_{\mu,\nu} \varphi_{\mu,\nu}(z_e), \quad (5)$$

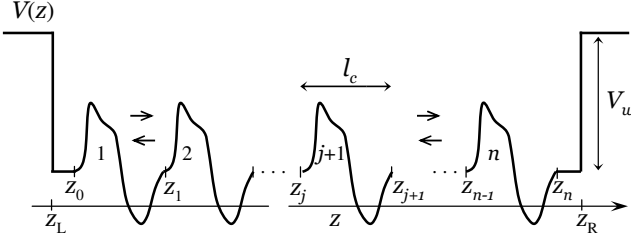


FIG. 2. Parameters of a quasi-bounded superlattice with arbitrary potential profile. The wave function in Eq. (13) is defined at any point z of the $j+1$ cell, with $0 \leq j \leq (n-1)$.

and

$$\left(-\frac{\hbar^2}{2m_h^*}\nabla_h^2 + V_h(z_h)\right)\varphi_{\mu',\nu'}(z_h) = E_{\mu',\nu'}\varphi_{\mu',\nu'}(z_h). \quad (6)$$

The wave functions for the Hamiltonian H_o can be written as

$$\Psi_i(\mathbf{r}_e, \mathbf{r}_h) = \varphi_{\mu,\nu}(z_e)\varphi_{\mu',\nu'}(z_h)\phi_j(\boldsymbol{\rho}_e, \boldsymbol{\rho}_h, z_e - z_h), \quad (7)$$

with $\phi_j(\boldsymbol{\rho}_e, \boldsymbol{\rho}_h, z_e - z_h)$ an eigenfunction of the quasi-two-dimensional Schrödinger equation

$$\left(\frac{\hbar^2}{2m_{||e}^*}\nabla_{||e}^2 - \frac{\hbar^2}{2m_{||h}^*}\nabla_{||h}^2 - V_{eh}(|\mathbf{r}_e - \mathbf{r}_h|)\right)\phi_j(\boldsymbol{\rho}_e, \boldsymbol{\rho}_h, z_e - z_h) = -E_j^{(2D)}\phi_j(\boldsymbol{\rho}_e, \boldsymbol{\rho}_h, z_e - z_h). \quad (8)$$

where $\nabla_{||i}$ is the in-plane component of the gradient with respect to the two-dimensional vector $\boldsymbol{\rho}_i$. A great deal of effort has been devoted in solving this equation, which provides the e - h pair binding energies.^{3,52,60,91-97} Although some consensus on the order of magnitude of these energies exists, more specific and accurate calculations for excitons in SLs are still lacking. We will take into account the existing results and, in the appendix, we will recall and extend the Leavitt-Little model to determine, also, the exciton binding energy in the first excited state. We shall now recall some useful results and relations related to the superlattice Schrödinger equations. For a simple discussion we will focus here on type I superlattices.

The SL might be open, bounded or quasi-bounded. Since most of the specific examples imply quasi-bounded SLs, we will restrict the detailed discussion to this kind of systems, but we will give also the selection rules in the other cases. General expressions for the evaluation of eigenvalues and eigenfunctions of the electron and hole SL Schrödinger equations (5) and (6), were given in Ref. [4]. It was shown that, provided the single cell transfer matrix

$$M(z_{i+1}, z_i) = \begin{pmatrix} \alpha & \beta \\ \beta^* & \alpha^* \end{pmatrix}, \quad (9)$$

is known, one can straightforwardly determine the n -cell transfer matrix elements, through the simple relations

$$\alpha_n = U_n - \alpha^* U_{n-1}, \quad \text{and} \quad \beta_n = \beta U_{n-1}, \quad (10)$$

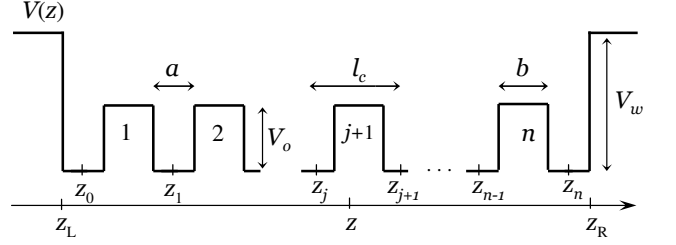


FIG. 3. Parameters of a quasi-bounded superlattice with sectionally constant barriers and wells. The wave function in Eq. (13) is defined at any point z of the $j+1$ cell, with $0 \leq j \leq (n-1)$.

where U_n is the Chebyshev polynomial of the second kind and order n , evaluated at the real part of $\alpha = \alpha_R + i\alpha_I$. The eigenvalues of any quasi-bound SL spanning from z_L to z_R in figure 2, with $z_0 - z_L = z_R - z_n = a/2$, can be obtained from

$$\Re(\alpha_n e^{ika}) - \frac{k^2 - q_w^2}{2q_w k} \Im(\alpha_n e^{ika}) - \frac{k^2 + q_w^2}{2q_w k} \beta_n = 0 \quad (11)$$

Here q_w and k are the wave numbers at the left (right) and right (left) of the discontinuity point z_L (z_R), and the eigenfunctions are given by

$$\Psi_{\mu,\nu}^{qb}(z) = \Psi^{qb}(z, E_{\mu,\nu}), \quad (12)$$

where

$$\Psi^{qb}(z, E) = \frac{a_o}{2k} \left[\left((\alpha_p + \gamma_p)\alpha_j + (\beta_p + \delta_p)\beta_j^* \right) e^{ika/2} (k - iq_w) + \left((\alpha_p + \gamma_p)\beta_j + (\beta_p + \delta_p)\alpha_j^* \right) e^{-ika/2} (k + iq_w) \right], \quad (13)$$

with a_o a normalization constant and z any point in the $j+1$ cell, i.e. any point between z_j and z_{j+1} , with $0 \leq j \leq (n-1)$. α_j, β_j, \dots are the matrix elements of the transfer matrix $M_j(z_j, z_0)$ that connects the state vectors $\Phi(z_0)$ and $\Phi(z_j = z_0 + jl_c)$, at points separated by exactly j unit cells, and α_p, β_p, \dots the matrix elements of the transfer matrix $M_p(z, z_j)$ that connects the state vectors $\Phi(z_j)$ and $\Phi(z)$, for $z_j \leq z \leq z_{j+1}$. In the particular case of a quasi-bounded periodic potential like the one shown in figure 3, the eigenvalues equation can be written as

$$h_w U_n + f_w U_{n-1} = 0 \quad (14)$$

with

$$\begin{aligned} h_w &= \frac{q_w^2 - k^2}{2q_w k} \sin ka + \cos ka, \\ f_w &= \frac{q_w^2 - k^2}{2q_w k} (\alpha_I \cos ka - \alpha_R \cos ka) - \alpha_R \cos ka \\ &\quad - \alpha_I \sin ka - \beta_I \frac{q_w^2 + k^2}{2q_w k}. \end{aligned} \quad (15)$$

and

$$\alpha = \cosh qb + i \frac{k^2 - q^2}{2kq} \sinh qb, \quad \beta = -i \frac{k^2 + q^2}{2kq} \sinh qb \quad (16)$$

The wave numbers in the various regions (wells, barriers and cladding layers) of the heterostructure, with the appropriate changes for electrons and holes in the conduction and valence bands, are: $k^2 = 2m^*E/\hbar^2$; $q^2 = 2m^*(V_o - E)/\hbar^2$ and $q_w^2 = 2m^*(V_w - E)/\hbar^2$. The potential parameters a , b , V_o and V_w are shown in figure 3. To simplify the notation we will write just $\Psi_{\mu,\nu}^q(z)$ for $\Psi_{\mu,\nu}^{qb}(z)$.

It was shown in Ref. [85] that writing the exciton field as

$$\begin{aligned}\Phi_{e-h}^r(z) &= \sum_{\mu,\nu} \Psi_{\mu\nu}^{r,c}(z) a_{\mu\nu} + \sum_{\mu',\nu'} \Psi_{\mu'\nu'}^{r,v}(z) b_{\mu\nu}^+ \\ &= \phi_c^r + \phi_v^{r+}\end{aligned}\quad (17)$$

with $a_{\mu\nu}$ and $b_{\mu\nu}$ the electron and hole annihilation operators and r a label to denote open (o), bounded (b) or quasi-bounded (q) SLs. The radiative interband (conduction to valence band) transition contribution of the exciton-field interaction $\langle \Phi_{e-h}^r(z) | H_I | \Phi_{e-h}^r(z) \rangle$ are given by

$$\langle \Phi_{e-h}^r(z) | H_I | \Phi_{e-h}^r(z) \rangle_{PL} = \int dz \phi_v^{r\dagger}(z) \mathbf{A} \frac{\partial}{\partial \mathbf{r}} \phi_c^r(z) \quad (18)$$

while the intraband (conduction to conduction band) transition contribution, of the infrared transitions (IR), by

$$\langle \Phi_{e-h}^r(z) | H_I | \Phi_{e-h}^r(z) \rangle_{IR} = \int dz \phi_c^{r\dagger}(z) \mathbf{A} \frac{\partial}{\partial \mathbf{r}} \phi_c^r(z) \quad (19)$$

Therefore, the photoluminescence spectrum of a superlattice in the active zone of light emitting devices is obtained, in the golden rule approximation, from

$$\chi_{PL}^r = \sum_{\nu,\nu',\mu,\mu'} f_{eh} \frac{\left| \int dz [\Psi_{\mu',\nu'}^{r,v}(z)]^* \frac{\partial}{\partial z} \Psi_{\mu,\nu}^{r,c}(z) \right|^2}{(\hbar\omega - E_{\mu,\nu}^c + E_{\mu',\nu'}^v + E_B)^2 + \Gamma^2} \quad (20)$$

$$\chi_{PL}^r = \sum_{\nu,\nu',\mu,\mu'} f_{eh} \chi_{\mu'\nu',\mu,\nu}^{r,PL} \quad (21)$$

with energies measured from the upper edge of the valence band. Here E_B is the exciton binding energy, Γ the

level broadening energy and f_{eh} the occupation probability, which in terms of the quasi-equilibrium distributions f_e and f_h , becomes⁶⁰

$$f_{eh} = 1 - f_e - f_h \propto \tanh \left[\frac{1}{2k_B T} (\hbar\omega - E_g - \mu_{eh}) \right] \quad (22)$$

where k_B is the Boltzmann constant, T the temperature and μ_{eh} the total chemical potential. At low temperatures f_{eh} is just a step function. In the same way, the infrared emissions spectrum is described by

$$\chi_{IR}^r = \sum_{\nu,\nu',\mu \geq \mu'} f_{eh} \frac{\left| \int dz [\Psi_{\mu',\nu'}^{r,c}(z)]^* \frac{\partial}{\partial z} \Psi_{\mu,\nu}^{r,c}(z) \right|^2}{(\hbar\omega - E_{\mu,\nu}^c + E_{\mu',\nu'}^c)^2 + \Gamma^2} \quad (23)$$

$$\chi_{IR}^r = \sum_{\nu,\nu',\mu \geq \mu'} f_{eh} \chi_{\mu'\nu',\mu,\nu}^{r,IR} \quad (24)$$

Since the wave functions $\Psi_{\mu,\nu}^r(z)$ possess well defined parities, as was shown in Ref. [6], the non vanishing contributions imply, for PL, the parity $P[\Psi_{\mu,\nu}]$ combinations

$$P[\Psi_{\mu',\nu'}^{r,v}] = \text{odd} \quad \text{and} \quad P[\Psi_{\mu,\nu}^{r,c}] = \text{even},$$

or

$$P[\Psi_{\mu',\nu'}^{r,v}] = \text{even} \quad \text{and} \quad P[\Psi_{\mu,\nu}^{r,c}] = \text{odd},$$

and similar relations for IR emissions, with c instead of v . Using these parity combinations, we will write in the next section a set of selection rules that will be referred to as *symmetry selection rules* (SSR), to distinguish from other empirical selection rules that will be reported in section 4, named *leading order rules* (LOR) and *surface and edge selection rules* (SESR), related to the intra-subband eigenfunctions' symmetries, briefly discussed in the Appendix A.

III. SYMMETRY SELECTION RULES

It was shown in Ref. [6] that the eigenfunctions of quasi-bounded SLs fulfill the symmetry relations

$$\Psi_{\mu,\nu}^q(z) = \begin{cases} (-1)^{\nu+1} \Psi_{\mu,\nu}^q(-z) & \text{for } n \text{ odd} \\ (-1)^{\nu+\mu} \Psi_{\mu,\nu}^q(-z) & \text{for } n \text{ even} \end{cases}. \quad (25)$$

This clearly leads to the following selection rules. When the number of unit cells n is even, the SSR are:

$$\int dz \Psi_{\mu',\nu'}^{q,v}(z) \frac{\partial}{\partial z} \Psi_{\mu,\nu}^{q,c}(z) \begin{cases} = 0 & \text{when } P[\mu' + \nu'] = P[\mu + \nu] \\ \neq 0 & \text{when } P[\mu' + \nu'] = P[\mu + \nu + 1] \end{cases} \quad (26)$$

while for n odd the SSR are

$$\int dz \Psi_{\mu',\nu'}^{q,v}(z) \frac{\partial}{\partial z} \Psi_{\mu,\nu}^{q,c}(z) \begin{cases} = 0 & \text{when } P[\nu'] = P[\nu] \\ \neq 0 & \text{when } P[\nu'] = P[\nu + 1] \end{cases} \quad (27)$$

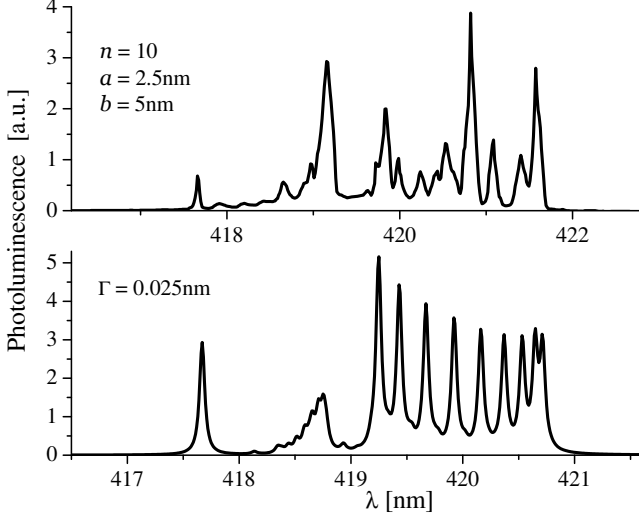


FIG. 4. Narrow peaks and subband groups in the PL spectra observed by Nakamura et al.^{55,98} (upper panel) and calculated with this paper's technique (lower panel) for the blue emitting heterostructure $GaN\backslash(In_{0.2}Ga_{0.8}N\backslash In_{0.05}Ga_{0.95}N)^n\backslash GaN$ with $n=10$, $a=2.5nm$ and $b=5nm$. The SL parameters considered here are shown in figure 5. The experimental spectrum is reproduced with permission from [Appl. Phys. Lett. **68**, 3269 (1996)]. Copyright [1996], AIP Publishing LLC.

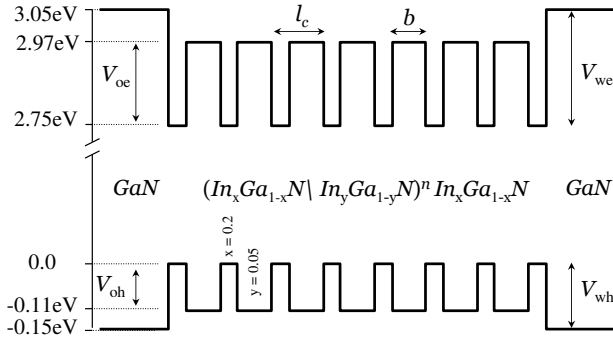


FIG. 5. Parameters of the $In_xGa_{1-x}N\backslash In_yGa_{1-y}N$ blue emitting superlattices used by Nakamura et al.⁵⁴

Similar relations are valid for IR transitions, with the additional restrictions $\mu \geq \mu'$ and, whenever $\mu = \mu'$, we must also have $\nu > \nu'$. The corresponding symmetry selection rules for open and bounded SLc are given in the appendix 1. These rules reduce effectively the number N of possible transitions by, at least, a factor $1/2$, i. e. to $N/2$. This is still a large number. In the next section we will introduce other rules and symmetries that reduce even more the number of matrix-elements evaluations. Before we present other rules, let us obtain some PL and IR spectra for specific examples using the SSR.

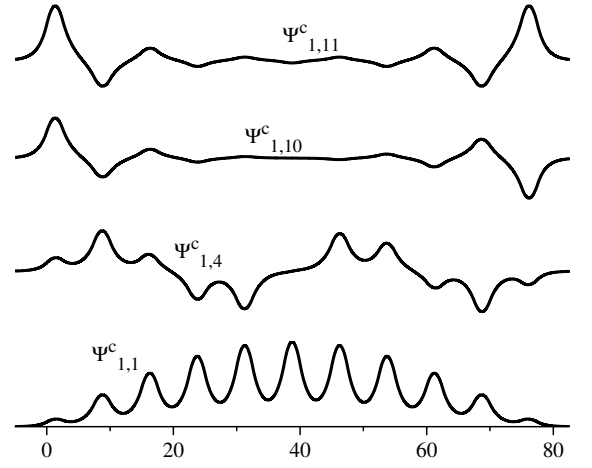


FIG. 6. The eigenfunctions $\Psi_{1,1}^{q,c}(z)$, $\Psi_{1,4}^{q,c}(z)$, $\Psi_{1,10}^{q,c}(z)$, and $\Psi_{1,11}^{q,c}(z)$ in the first subband of the conduction band of the blue emitting heterostructure $(In_{0.2}Ga_{0.8}N\backslash In_{0.05}Ga_{0.95}N)^{10}\backslash In_{0.2}Ga_{0.8}N$, bounded by GaN cladding layers, with $a=2.5nm$ and $b=5nm$.

III.1. PL of blue emitting devices. Nakamura's results

As the first example we choose a SL with the highest PL spectra accuracy that we could find in the literature. Nakamura et al. reported PL measurements with resolutions of the order of $0.016nm$,⁹⁸ for the blue emitting $GaN\backslash(In_xGa_{1-x}N\backslash In_yGa_{1-y}N)^n\backslash GaN$ SLs, with n varying between 3 and 20, for $x=0.2$ and $y=0.05$. In the upper panel of figure 4, we reproduce the experimental PL spectrum, for $n = 10$. An important characteristic of this spectrum is the presence of narrow peaks, clustered in groups. In Nakamura's words "it was not clear which was the origin" of these narrow peaks.⁹⁸ Nakamura et al. suggested, that they could originate in the "sub-band transition between quantum energy levels caused by quantum confinement of electrons and holes".⁹⁸ Our calculations, in the lower panel of figure 4, and the analysis below, show that this is precisely the origin. The spacing and number of narrow-peaks and groups, correspond with the spacings of the energy-levels and of the surface states in the subbands of the conduction and valence bands.

Before we discuss our results, let us briefly sketch the steps followed for the evaluation of the photoluminescence spectrum for a given SL: i) we fix input parameters like the well and barrier widths, gap energies, the spin split off and the effective masses; ii) using equations (12) and (13) and (14), we get the eigenvalues and the eigenfunctions; iii) we normalize the eigenfunctions and evaluate the transition matrix elements, allowed by the selection rules, and iv) we plug the transition matrix elements and eigenvalues in the optical response of Eq. (20). In Table 1 we show the energy eigenvalues $E_{1,\nu}$ in the first subband, of the conduc-

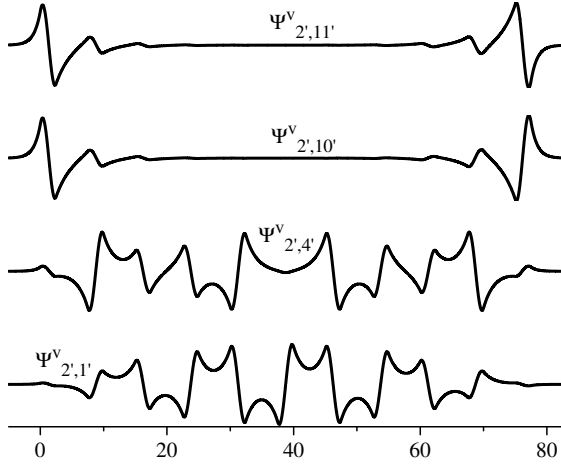


FIG. 7. The eigenfunctions $\Psi_{2,1}^{q,v}(z)$, $\Psi_{2,4}^{q,v}(z)$, $\Psi_{2,10}^{q,v}(z)$, and $\Psi_{2,11}^{q,v}(z)$ in the second subband of the valence band of the blue emitting heterostructure $(\text{In}_{0.2}\text{Ga}_{0.8}\text{N}/\text{In}_{0.05}\text{Ga}_{0.95}\text{N})^{10}/\text{In}_{0.2}\text{Ga}_{0.8}\text{N}$, bounded by GaN cladding layers, with $a=2.5\text{nm}$ and $b=5\text{nm}$.

tion band and the eigenvalues $E_{2',\nu'}$ for heavy holes in the second subband of the valence band, when the SL is $(\text{In}_x\text{Ga}_{1-x}\text{N}/\text{In}_y\text{Ga}_{1-y}\text{N})^n/\text{In}_x\text{Ga}_{1-x}\text{N}$ with $x=0.2$, $y=0.05$ and $n=10$, bounded by GaN cladding layers. Notice that the eigenvalues $E_{1,10}$, $E_{1,11}$, $E_{2,10}$ and $E_{2,11}$, darkened in the Table are slightly detached. As was shown in Ref. [4], these energy levels correspond to surface states. In figures 6 and 7 we plot the eigenfunctions $\phi_{1,\nu}$ and $\phi_{2',\nu'}$ for $\nu, \nu'=1, 4, 10$ and 11 . The last two are clearly surface states.

Table 1: Energy eigenvalues $E_{1,\nu}^c$ and $E_{2',\nu'}^v$ for the SL $(\text{In}_{0.2}\text{Ga}_{0.8}\text{N}/\text{In}_{0.05}\text{Ga}_{0.95}\text{N})^{10}/\text{In}_{0.2}\text{Ga}_{0.8}\text{N}$ bounded by GaN cladding layers

μ	ν	$E_{\mu,\nu}^c - E_g$	μ'	ν'	$E_{\mu',\nu'}^v$
	1	0.101951282609	1		-0.092052406590
	2	0.1027359799442	2		-0.092251334829
	3	0.1040047691302	3		-0.092572604852
	4	0.1056959172240	4		-0.092999723475
	5	0.1077167669465	5		-0.093507350719
1	6	0.1099379875843	2'	6	-0.094058967290
	7	0.112187139073	7		-0.094604303220
	8	0.1142406480441	8		-0.095078402370
	9	0.1158006914057	9		-0.095407111300
	10	0.119074068840	10		-0.10012439720
	11	0.119082083156	11		-0.10012440024

The experimental⁹⁸ and theoretical PL spectra of this sample, with $n=10$, are shown in figure 4. Similar results are shown in figure 8 for $n=7$. The theoretical calculations, plotted in the lower panels, should be compared with the experimental results in the upper panels.

To understand the structure of the optical response in figures 4 and 8, we need first to recall that in bounded and quasi bounded system, two of the $n+1$ eigen-energies

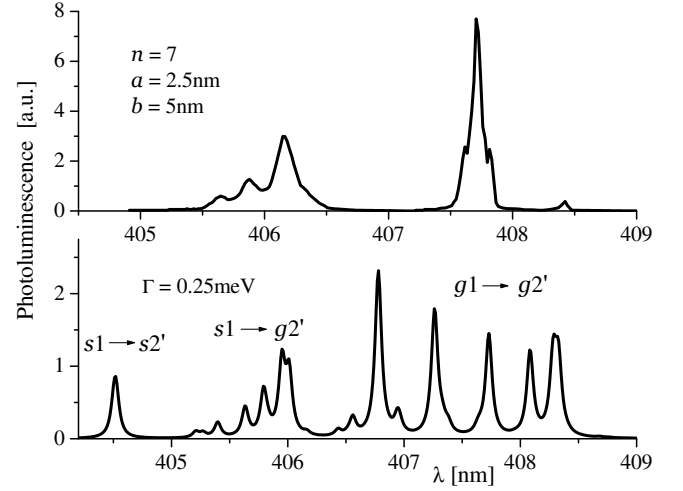


FIG. 8. Narrow peaks and subband groups in the PL spectra observed¹⁰² (upper panel) and calculated (lower panel) for a blue emitting heterostructure $\text{GaN}/(\text{In}_x\text{Ga}_{1-x}\text{N}/\text{In}_y\text{Ga}_{1-y}\text{N})^n/\text{GaN}$ with $n=7$. The SL parameters considered here are as in figure 3 but with different bowing parameters.

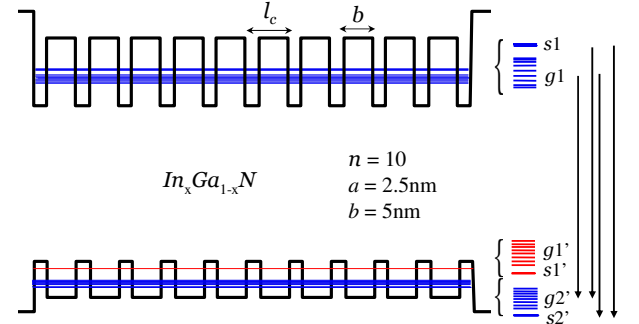


FIG. 9. Parameters for the blue emitting heterostructure $\text{GaN}/(\text{In}_x\text{Ga}_{1-x}\text{N}/\text{In}_y\text{Ga}_{1-y}\text{N})^n/\text{GaN}$.

$E_{\mu,\nu}$ are surface states SS , which, as was shown in Ref. [4] and can be seen in Table 1, detach from the remaining $n-1$ grouped states with a detachment energy that depends on the height of the lateral potentials. To simplify the reference to these states let us denote the surface states in a subband μ as $\{s\mu\}$ and the grouped states as $\{g\mu\}$. Similarly, in the valence band we have the sets $\{s\mu'\}$ and $\{g\mu'\}$, see figure 9. For the SL with the PL spectra of figure 4, we have one subband in the conduction band and two subbands in the valence band. The surface states in the set $s1$, for the energy eigenvalues $E_{1,10}=0.119074\text{eV}$ and $E_{1,11}=0.119082\text{eV}$, measured from the band edge, are detached 3.2meV from the the set $g1$, grouped in an energy interval of 13.9meV. The first subband of the valence band is extremely thin, the set $g1'$ is located around -0.026eV, and the SS $s1'$ at -0.028eV. This subband is so thin that, it is easy to miss it. The set $g2'$ of the second subband contains energy levels $E_{2',\nu'}$ between -0.092eV and -0.0954eV, and the set $s2'$

is located around -0.1001244eV. The transitions sketched in figure 9 are transitions to the second subband of the valence band. The transitions to the first subband are negligible. In figures 4 and 8 we have, basically, the following transitions: $g1 \rightarrow g2'$, responsible for the group of peaks to the right of the figure, with larger λ s; the transitions $s1 \rightarrow g2'$, responsible for the group in the middle and the transitions $s1 \rightarrow s2'$ responsible for the almost isolated peak at the left. The transitions $g1 \rightarrow s2'$ are immersed in the group of peaks in the middle.

For this spectrum, all the matrix elements allowed by symmetry selection rules were considered. This means $N/2 \simeq 120$ matrix elements. The theoretical spectrum, based on the SL parameters shown in figure 4, is slightly shifted to smaller wavelengths. A small difference like this can be fitted adjusting parameters like the energy gaps, but this is not the goal now. Our purpose is to stress the ability of the theoretical calculations to account for subtle features like the peaks separations and the group structure. It is worth noticing that, notwithstanding the lack of symmetry of the blue emitting SL devices, which have a GaN layer on one side and an $Al_{(0.2)}Ga_{0.8}N$ layer on the other, the agreement is rather good, except for SLs with a small number of unit cells, where taking into account the asymmetry helps. In fact, if we consider the SL $GaN \setminus (In_{0.2}Ga_{0.8}N \setminus In_{0.05}Ga_{0.95}N)^n \setminus Al_{0.2}Ga_{0.8}N$ with $n = 7$, and compare with the symmetric one, we have, related with the eigenfunctions characteristics, that while the low lying eigenfunctions of the asymmetric and symmetric SLs (shown in the lower panel of figure 10) almost coincide, the high energy eigenfunctions (shown in the upper panel) differ. In general the asymmetry effect is larger on the surface states rather than in the low lying ones; the surface energy levels detach further and the particles get also localized. The PL spectrum of the asymmetric SL $GaN \setminus (In_{0.2}Ga_{0.8}N \setminus In_{0.05}Ga_{0.95}N)^7 \setminus Al_{0.2}Ga_{0.8}N$, is shown in figure 11. The structure reflects the fact that one of the two, almost degenerate, surface states in $\{s1\}$ is pushed up, about 15meV, while the other states remain practically in the same position. Because of this splitting in s_1 , instead of the transitions $s1 \rightarrow g2'$, we have now two groups: the transitions $E_{1,7} \rightarrow g2'$ and the transitions $E_{1,8} \rightarrow g2'$, each with three peaks. At the same time the large peak, due to the $s1 \rightarrow s2'$ transition, practically disappears, as can also be seen in the experimental spectrum.

It is worth noticing, however, that even though the range of predicted wavelengths for the PL peaks is of the order of the observed ones, using either the gap energy $E_{g,GaN} = 3.4$ or $E_{g,GaN} = 3.2$, with the appropriate bowing parameter in $E_g(x) = x1.95 + (1-x)E_{g,GaN} - Bx(1-x)$, a better agreement is found when the energy gap of the cubic (zincblende) structure, $E_{g,GaN} = 3.2$, is taken into account.⁹⁹

An important feature in the PL spectra, particularly in the low resolution measurements, is the relatively small

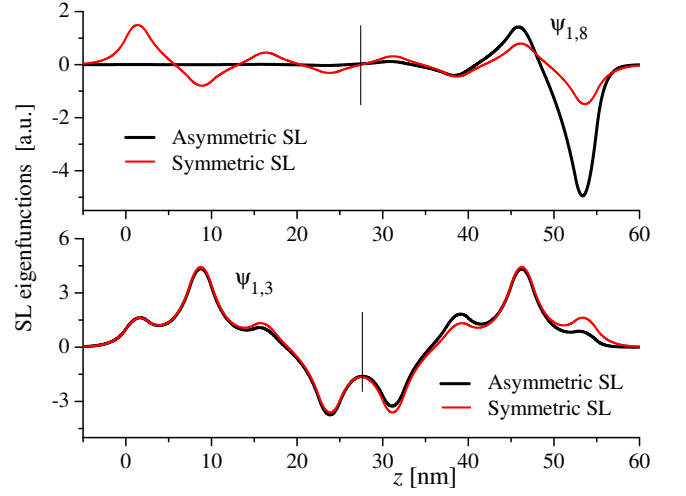


FIG. 10. Eigenfunctions of symmetric (red) and asymmetric (black) lateral barriers in the $(In_{0.2}Ga_{0.8}N \setminus In_{0.05}Ga_{0.95}N)^n$ SL with $n=7$. The asymmetry effect is larger on the surface states.

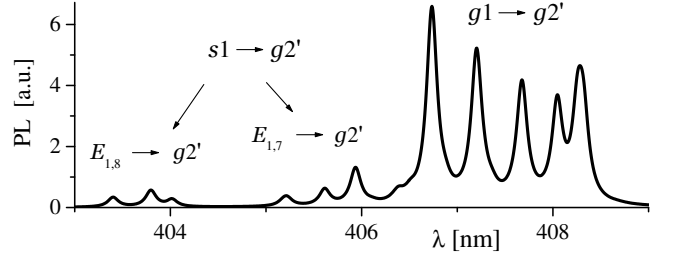


FIG. 11. The PL spectrum when the asymmetry of the lateral-barriers height is taken into account. As the surface states are split and pushed up further, the peaks due to transitions $s1 \rightarrow g2'$, in the lower panel of figure 8, also split, and the agreement with the experimental PL, around $\lambda=406$ nm, improves.

number of peaks. This leads us to recognize other rules that will be introduced in the next sections, which pick up matrix elements that contribute more to the PL and the IR spectra.

III.2. Infrared transitions

Let us now consider IR spectra for another kind of SLs where the surface energy levels do not detach from the other subbands or minibands. This happens when the semiconductor in the cladding layers is the same as that of the barrier. Helm et al.^{46,100,101} produced $(Al_{0.3}Ga_{0.7}As \setminus GaAs)^n \setminus Al_{0.3}Ga_{0.7}As$ SLs with a large number of unit cells ($n=200, 400$ and 500) and valley and barrier widths of a few nanometers up to 40nm. They measured the IR spectra and based on these results together with the golden rule plus the dispersion relations (calculated from the Kronig-Penney model), they were able to infer the density of states in the minibands as

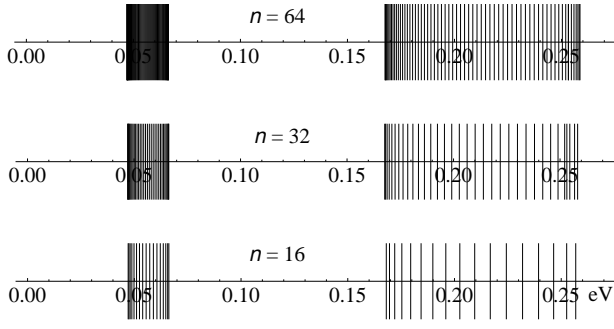


FIG. 12. Subbands of energy eigenvalues in the conduction band of the $(Al_{0.3}Ga_{0.7}As/GaAs)^n$ SL. The subband widths are independent of the number of unit cells n ; as n grows, the energy-eigenvalues densities become essentially the same up to a constant factor.

well as the oscillator strengths. We will now show that being able to explicitly evaluate the transition matrix elements, the experimental spectra can be accounted for without experimental parameters and without assumptions on oscillator strengths.

Before we present our results it is worth to recall and to stress some important properties related with the subband widths and the density of states. It is well known that the band widths, determined in the TFPS by the trace of the single cell transfer matrix, i.e. by $\text{Tr}M/2 \leq 1$, do not change when the number of unit cells n varies from, say, $n=20$ to $n=30$ or to $n=500$. This can be seen in figure 12 where the energy spectra of $(Al_{0.3}Ga_{0.7}As/GaAs)^n/Al_{0.3}Ga_{0.7}As$ is plotted for $n=16, 32$ and 64 . It was shown in Ref. [83] that in the large n limit, the density of energy eigenvalues agrees with the density of states in the continuum derived by Kronig and Penney. It is then clear that, once the energy eigenvalues are obtained, their spacings define implicitly the actual density of states, and the matrix elements (of the electron-field interaction) define, in principle, the so called oscillator strengths. We will show below that the IR spectrum of a SL with $n=20$ is the same as that for $n=30$, and describes quite well the experimental spectrum of a SL with $n=200$. Therefore, producing SLs with 200 or 500 periods, will no longer be necessary, though it helped to justify the use of a theory for infinite periodic systems.

For the calculation of the IR spectrum based on the golden rule (23) we use again the symmetry selection rules (26) and (27), with $\Psi_{\mu',\nu'}^{q,v}(z)$ replaced by $\Psi_{\mu',\nu'}^{q,c}(z)$. As for the PL, the calculation is simple and direct when the energy eigenvalues $E_{\mu,\nu}$ and the corresponding eigenfunctions $\Psi_{\mu,\nu}$ are known.

In figure 13 we show both an experimental result (upper panel) reported in Refs. [46], [100], and [101], and our theoretical calculation (lower panel). The IR absorption was measured for the $(Al_{0.3}Ga_{0.7}As/GaAs)^n/Al_{0.3}Ga_{0.7}As$ SL with valley and barrier widths of 7.5nm and 2.5nm, respectively, and for

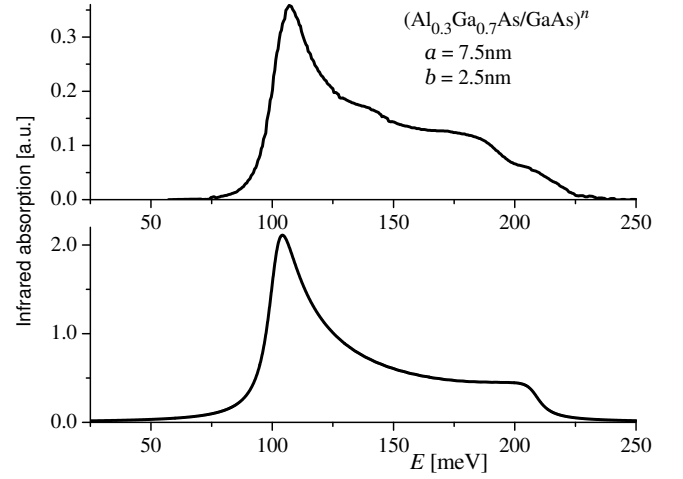


FIG. 13. The IR absorption spectrum measured by Helm et al.^{46,100,101} (upper panel), and the theoretical calculation for the $(Al_{0.3}Ga_{0.7}As/GaAs)^n/Al_{0.3}Ga_{0.7}As$ SL with valley and barrier widths of 7.5nm and 2.5nm. The experimental spectrum is reproduced here with permission of the author.

a number of periods of the order of 200. If we consider $n=200$, the number of matrix elements that we need to evaluate would be of the order of 40,000. A huge number. The experimental accuracies were, apparently, of the order of 2-3meV and the samples were lightly doped. For our theoretical calculations we use the same potential parameters as in Ref. [100], and taking into account the arguments just explained, we considered samples with smaller number of unit cells. Indeed, for the IR spectra in figure 13 we had $n=31$. In figure 14, we show the IR spectra for $n=21$, implying the evaluation of 240 matrix elements. The results are practically equivalent. It is worth noticing that in the theoretical calculation by Helm et al., based on the Kronig Penney model, the first subband ranges from 37 to 55meV and the second from 148 to 222meV. In our calculation (see figure 12), the first subband ranges from 47 to 66meV and the second from 168 to 254meV. This implies an IR spectrum that extends from 102meV to 207meV, which is precisely the energy interval where the observed IR and the theoretical spectrum for $\Gamma=0.005\text{eV}$ lie.

III.3. PL spectra for $(Al_xGa_{1-x}As/GaAs)^n$ SLs. Exciton binding energies

Absorption and PL spectra for $(Al_xGa_{1-x}As/GaAs)^n$ SLs were measured long ago by many people, among others: Dingle et al.,¹¹ Miller et al.,¹³ Molenkamp et al.⁴⁵ and Masselink et al.⁵⁰ In most of the multi quantum well structures considered in those years, the barrier widths were extremely large, of the order of 20 or 30nm, with rather narrow valley widths, of the order of 5nm. The number of unit cells were also extremely large, 100 up to 400. The purpose was to produce a

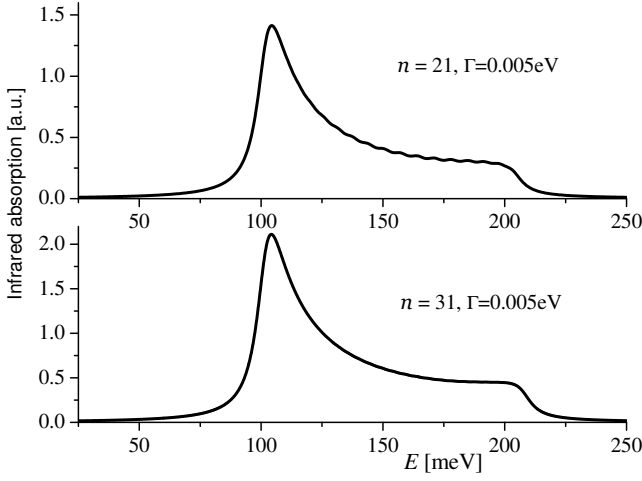


FIG. 14. Calculated IR spectra for the experimental data of figure 13. For these plots we considered $n=21$ (upper panel) and $n=31$ (lower panel). The results are practically the same.

large number of independent quantum wells. We are not going to discuss much on these type of SLs, we will instead study below, with more detail, the PL spectrum of $(Al_xGa_{1-x}As/GaAs)^n$ SLs with thinner barrier widths. Wide and high barriers lead to almost independent single quantum wells and to extremely narrow minibands, difficult to find and to evaluate theoretically. A rigorous calculation of the miniband structure for the sample 4-10-74 of Dingle et al., with $x=0.2$, valley width of 9.2nm and barrier width of 34.5nm, gives a first miniband with $E_{1,1}$ at 0.0363318072eV, above the CB edge, and $E_{1,n+1}$ at 0.0363318085eV. This means a subband width of 13×10^{-7} meV. Thus, extremely narrow minibands on top of a wide background. In this class of systems the theoretical calculation of surface states is also numerically unstable.

Masselink et al.⁵⁰ considered samples with thinner barriers and wider wells. Although this, in principle, implies a larger number of subbands, with subband-widths of the order of 10meV, the theoretical calculations are feasible. In the upper panel of figure 15 we show the spectrum reported by Masselink et al. for the SL $(Al_{0.25}Ga_{0.75}As/GaAs)^n/Al_{0.25}Ga_{0.75}As$ with $a=21$ nm, $b=10$ nm and superlattice-thickness of the order of 1 to 2 μ m. This means SLs with n of the order of 50. In this sample, because of the wide valley width, there is a large number of subbands both in the CB and the VB. For energies below the barrier heights, the CB contains 4 subbands; the VB contains 6 heavy-hole subbands and 3 light-hole subbands. The subband widths are, generally, smaller than 10meV. Besides the large density of subbands, there is also a high density of energy levels in the subbands. Thus, in the actual spectrum, with accuracies much larger than 0.1meV, the single transitions peaks overlap. In the theoretical calculations there is no problem resolving the subband structures. To avoid the huge number of matrix elements and, as discussed before,

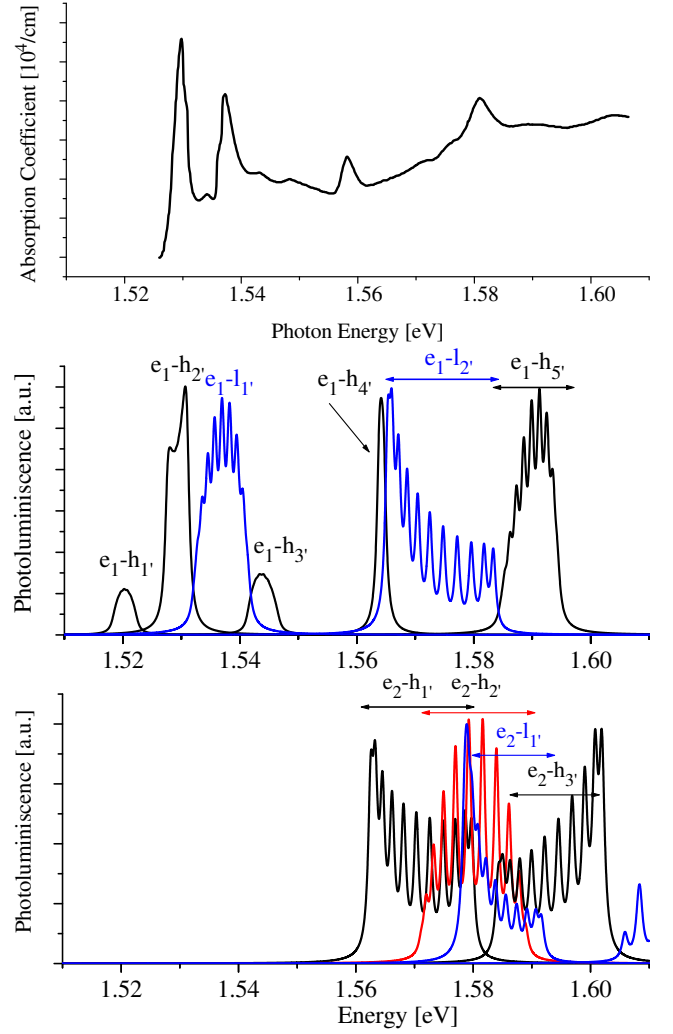


FIG. 15. In the upper panel absorption spectra reported by Masselink et al. for one of the $(Al_xGa_{1-x}As/GaAs)^n$ SLs, with well width $w=15$ nm barrier width $b=2.5$ nm and SL length of the order of 1 μ m. The panel in the middle contains only the transitions $e_{1\nu}-hh_{\mu'\nu'}$ (black) and $e_{1\nu}-lh_{\mu'\nu'}$ (blue), denoted as $e_1-h_{\mu'}$ and $e_1-l_{\mu'}$ (with origin in the first subband of the CB), and in the lower panel, the transitions $e_{2\nu}-hh_{\mu'\nu'}$ and $e_{2\nu}-lh_{\mu'\nu'}$ starting in the second subband of the CB. For these graphs, only the ground state exciton binding energy was considered.

without any relevant change in the results we consider n of the order of 10.

In the lower panels of figure 15 we present the theoretical calculations, black and red curves for $e-hh$ transitions and blue for $e-lh$ transitions. To visualize better the peaks of the possible contributions, the panel in the middle contains only the transitions $e_{1\nu}-hh_{\mu'\nu'}$ (black) and $e_{1\nu}-lh_{\mu'\nu'}$ (blue), denoted as $e_1-h_{\mu'}$ and $e_1-l_{\mu'}$, with initial state in the first subband of the CB, and in the lower panel, the transitions $e_{2\nu}-hh_{\mu'\nu'}$ and $e_{2\nu}-lh_{\mu'\nu'}$ starting in the second subband of the CB. For these graphs, only the exciton binding energy in the ground state was con-

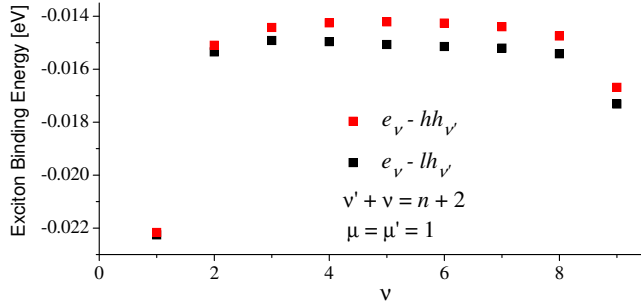


FIG. 16. Binding energies obtained for the superlattice $(Al_xGa_{1-x}As/GaAs)^n$ considered in figure 15, after evaluating the excitons size $[\langle \mu', \nu' | (z_e - z_h)^2 | \mu, \nu \rangle]^{1/2}$ and assuming quasi-spherical excitons.

sidered. The transitions $e_{1\nu}-hh_{1\nu'}$ and $e_{1\nu}-hh_{3\nu'}$, denoted $e_1-h_{1'}$ and $e_1-h_{3'}$ in the upper graph, have been multiplied by large factors to make them visible.

Before we comment our results, it is worth stressing again the important difference between this approach and the standard one. In the experimental reports it is rather frequent to find statements related with the observation of “forbidden transitions”.^{45,49–53} Forbidden in the standard approach where only one index μ defines the “subband wave function” parity. In the TFPS there is no such thing like the “subband wave function”. As we have already seen, the subbands in the TFPS contain many intrasubband levels (all of them with their corresponding eigenfunction characterized by two indices) which, together with the number of unit cells, define the selection rules. Therefore, transitions with subband indices $\mu \neq \mu'$, forbidden in the standard theory, are perfectly possible in this TFPS. In our plots, the occupation probability is assumed as a step function. No Sommerfeld effect is considered, but the exciton binding energy was taken into account. The 2D exciton binding energy was evaluated, as explained in the Appendix 1, from

$$E_{Bi} = -\frac{\alpha_{ri}^2 \hbar^2}{8m_r} \quad \text{with} \quad \alpha_{ri} = \frac{m_r e^2}{2\pi \epsilon \hbar^2 \lambda_i}, \quad (28)$$

where m_r is the relative mass, ϵ the dielectric constant and λ_i the quantum number with values $\lambda_0 = 1/2$ and $\lambda_1 = 3/2$, for the ground and excited 2D exciton states, respectively. Using these energies (-18meV for hh and -12meV for lh , in the ground state) the agreement with the experimental measurements is good. However, had we considered binding energies of the order of -10meV,^{38,49,51,92,93,103} the agreement would have not been that good.

To confirm the order of magnitude of the binding energies used here, we did the following exercise. Using the SL eigenfunction, we obtain on one side the mean positions $\langle \mu', \nu' | z_e | \mu, \nu \rangle = \langle \mu', \nu' | z_h | \mu, \nu \rangle = 0$, when the origin is in the center of the SL, and, on the other side, the exciton size along the SL from $[\langle \mu', \nu' | (z_e - z_h)^2 | \mu, \nu \rangle]^{1/2}$. Assuming quasi-spherical excitons, the binding energies take the values shown in figure 16. Although the order of

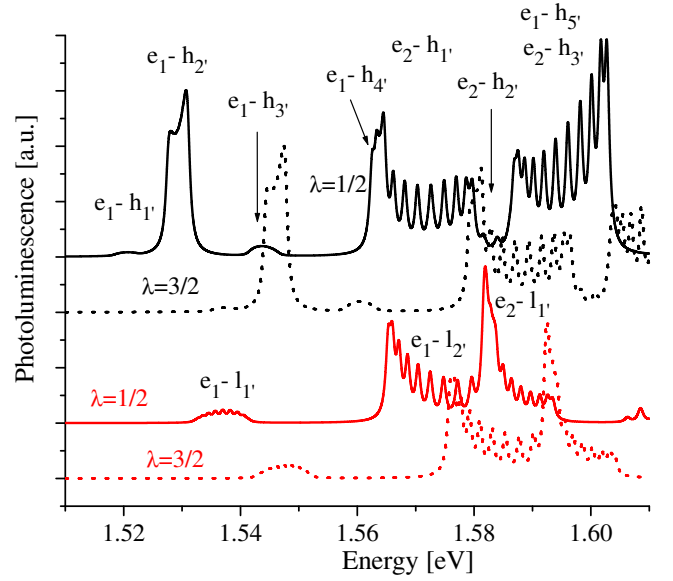


FIG. 17. In this figure we show again the optical transition for the superlattice $(Al_xGa_{1-x}As/GaAs)^n$ considered in figure 15. Together with the 2D excitonic ground state transition (full curves) we plot also those of the first excited 2D exciton state (dashed curves). In the uppermost graphs (black curves) we have the $e-hh$ transitions, denoted as $e_\mu-h_{\mu'}$, and in the lower graphs (red curves) we have the $e-lh$ transitions, denoted as $e_\mu-l_{\mu'}$. The binding energies in the 2D exciton ground state ($\lambda=1/2$) are 0.01877meV and 0.01187meV for heavy and light holes, while in the excited state ($\lambda=3/2$) they are 0.0021meV and 0.0013meV, for heavy and light holes respectively.

magnitude of these energies is correct, we just considered the binding energies from Eq. (28).

In figure 17 we plot, besides the ground state transitions (full curves), transitions from the first excited excitonic states (dotted curves). Within each graph of this figure, we respect the relative magnitudes except for the transitions $e_1-h_{1'}$ and $e_1-h_{3'}$ that were again enhanced in order to visualize them. The transitions from the excited excitonic states spectra that we would like to notice are those corresponding to $e_1^*-h_{2'}^*$, around 1.547eV, and $e_1^*-h_{3'}^*$, around 1.56eV, because these may explain those peaks in the experimental spectrum, above 1.54eV and below 1.56eV.

Let us now comment a couple of interesting issues. The resonances lineshapes for transitions like $e_\mu-h_{\mu'}$ or $e_\mu-l_{\mu'}$ have some interesting characteristics. We found that when the subband indices μ and μ' are both even or both odd the spectrum has a bell shape, however when they have different parities, see figure 18, the spectrum has, depending on the level broadening energy Γ , a U shape or a trapezoidal shape, with higher peaks at the left or right of the spectrum. For larger Γ or low experimental accuracy, the spectrum looks as having two peaks; see for example the spectrum for $e_1-h_{2'}$. This kind of results and behavior lead easily to wrong assignments of subband-indices. Spectrum shapes like these are fre-

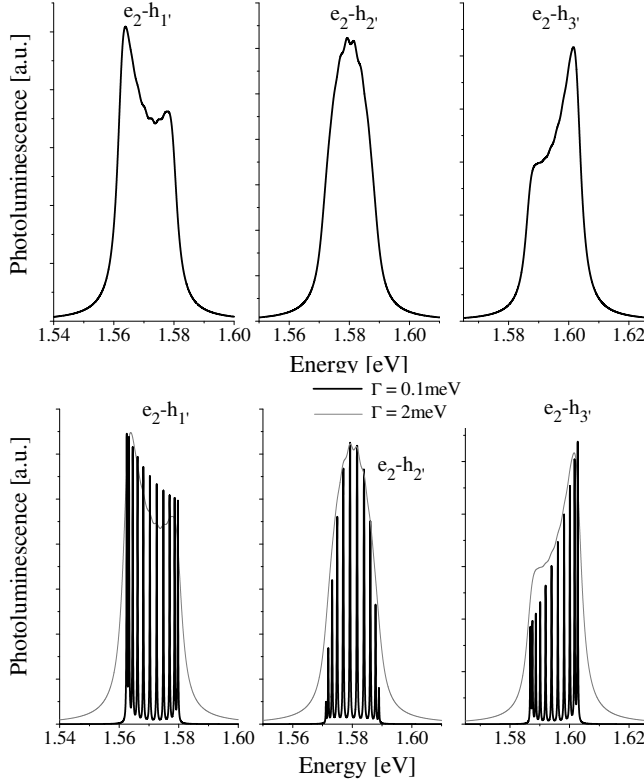


FIG. 18. Lineshapes of the transitions $e_2-h_{\mu'}$ shown in the lower frame of figure 15, plotted here for two values of the level broadening energy Γ . In the upper graphs we employed $\Gamma=2\text{meV}$ while in the lower graph we plot for both $\Gamma=0.1\text{meV}$ and $\Gamma=2\text{meV}$. This makes clear that with low accuracy experiments and calculations the intrasubband structures disappear. These transitions, experimentally observed, are forbidden in the standard theory.

quent in the literature. For example, the absorption coefficients reported by Helm et al in Refs. [46,101]. In these references the two maxima are considered critical points of the mini-Brillouin zone and, to fit the curves, it was necessary to assume oscillator strengths of the order of 0.3 at the center and 2.3 at the edge of the Brillouin zone.⁴⁶ In the PL spectra of figure 17, the subband widths ΔE_2^c and ΔE_3^c , of the second and third subbands in the CB, are $\simeq 0.018\text{eV}$ and 0.043eV , respectively, while the first four subbands in the VB lie between $\simeq 0.00293\text{eV}$ and $\simeq 0.0274\text{eV}$. Due to these characteristics, the interband transitions $e_2-h_{1'}$, $e_2-h_{2'}$ and $e_2-h_{3'}$ overlap. Thus, we can have, for example, peaks of $e_2-h_{2'}$ transitions at higher energies than peaks of the transitions $e_2-h_{3'}$, see lower panel in figure 15. In the Kronig-Penney like approach of Masselink et al., the fulfilment of boundary conditions for even and odd solutions in the valley and barrier led to an "eigenvalue equation", that generalizes, slightly, the single quantum well eigenvalue equation. This is not of course the correct eigenvalue equation for a superlattice. Although the eigenvalues E_μ may lie inside the subband μ , one can not define with them the

subband widths $\Delta\mu=E_{\mu,n+1}-E_{\mu,1}$.

As mentioned before, a peculiar and rather general characteristic of most of the published and calculated PL and IR spectra, is the small number of peaks, much smaller than the $N/2$ non-vanishing optical transitions. One reason is of course the low experimental precision. However, a closer look to the numerical values of the allowed matrix elements $\chi_{\mu'\nu',\mu\nu}^{r,PL} = \langle \mu', \nu' | \frac{\partial}{\partial z} | \mu, \nu \rangle$, shows that most of them are negligible, and only a small fraction, the leading order transitions (LOT), determine the shape of the optical spectrum and lead to new rules, related with the intraband eigenfunction's symmetry noticed in Ref. [4]. This fact motivates the discussion and content of the next section. We will repeat the PL calculations for the SL in the first example of this section and we will perform PL and IR calculations for other systems as well. The purpose is to show that, besides the SSR mentioned in this section, there are other rules that can be introduced without changing significantly the PL spectrum. Using the new rules we will obtain practically the same PL and IR spectra, with much less effort. They can be extremely useful when the number of subbands is large, say, two, three or more, and the number of cells is large.

IV. THE INTRABAND SYMMETRIES. LEADING ORDER RULES

Analysis of the matrix-elements for a large number of specific examples shows generally that the matrix elements $\langle \mu', \nu' | H_I | \mu, \nu \rangle$ where the parity of the index μ is the same as that of μ' are one or more orders of magnitude smaller than the others. This means, for example, that

$$\langle 1', \nu' | H_I | 1, \nu \rangle \ll \langle 2', \nu' | H_I | 1, \nu \rangle$$

or

$$\langle 3', \nu' | H_I | 1, \nu \rangle \ll \langle 2', \nu' | H_I | 1, \nu \rangle.$$

On the other hand, when the eigenfunctions $\Psi_{\mu,\nu}$ of a given subband are plotted for $\nu=1, 2, \dots, n+1$, we can find, as noticed in Ref. [4], another symmetry. We find that the envelope of $\Psi_{\mu,\nu}$ is similar to that of $\Psi_{\mu,n-\nu}$, when the surface energy levels are detached, and similar to that of $\Psi_{\mu,n+2-\nu}$ when the surface levels do not detach; see the appendix A. This eigenfunction symmetry related to the intraband indices ν and ν' together with the parities of μ and μ' define new rules that help to determine the matrix elements that are two or more orders of magnitude greater. When the potential height in the cladding layers is larger than the barrier height in the SL, and the surface states separate significantly, the matrix

elements that fulfill the conditions

$$\langle \mu', \nu' | \frac{\partial}{\partial z} | \mu, \nu \rangle \text{ with } \begin{cases} |\mu - \mu'| = 1, 3, 5, \dots \\ \text{and} \\ \nu + \nu' = n \\ \nu = n, n+1 \quad \nu' = 1, 2, \dots \\ \nu' = n, n+1 \quad \nu = 1, 2, \dots, \end{cases} \quad (29)$$

besides the SSR, are the leading order transitions. But when the potential height is comparable with the barrier height in the SL, the leading order transitions correspond to matrix elements satisfying the rules

$$\langle \mu', \nu' | \frac{\partial}{\partial z} | \mu, \nu \rangle \text{ where } \begin{cases} |\mu - \mu'| = 1, 3, 5, \dots \\ \text{with} \\ \nu + \nu' = n, n+2 \end{cases} \quad (30)$$

in addition, of course, of the SSR. These rules that will be referred to as the leading order rules (LOR) reduce the number of evaluations for PL from $N/2 \simeq (n+1)^2 n_c n_v / 2$ to $nn_c n_v / 2$ in the first case (equation 29), and to $(n+1)n_c n_v / 2$ in the last one (equation 30). Generally the experimental results show only a part of the spectra, accordingly the number of evaluations for a given plot is also a fraction of these numbers. Therefore, in the following the actual number of evaluations behind each plot depends on how many subbands of the conduction and valence bands are taken into account. For IR transitions we have the additional condition $\mu' \leq \mu$. The number of evaluations is reduced also significantly.¹⁰⁴

As an example of the first case we can consider the blue emitting system studied in the last section. For this system, with $n_c = n_v = 2$ and $n = 10$, the number of matrix evaluations reduces from $(n+1)^2 n_v / 2 = 121$ to $nn_v n_c / 2 = 20$. In figure 19, we plot the spectra with and without the LOR. The spectrum in the lower panel contains, essentially, the same information as that in the upper one.

Among the large amount of results reported in the literature for the IR spectrum of the $(GaAs/Al_x Ga_{1-x} As)^n$ SL, let us consider the SL with $x = 0.3$, valley width $a = 40\text{nm}$ and barrier width $b = 5\text{nm}$, studied in Ref. [31]. The length of this SL was $6\mu\text{m}$, which means $n \simeq 133$. If we consider a SL with this number of unit cells, the number of allowed IR transitions will be about 140,000, for $n_c = 4$. But, as mentioned above, the same physics comes out when the number of unit cells is, say, of the order of 10. It is worth recalling that since the actual SL in Ref. [31] was highly impurified, additional peaks appeared in the experimental results. Because of the large well width in these samples, the number of subbands is large, and the subband positions and widths are extremely sensitive to potential parameters and effective masses. Assuming a cladding layer with $x = 0.45$ and parameters from Ref. [105], we calculated accurately the relevant n of the $n+1$ energy eigenvalues and eigenfunctions for each of the first four subbands, both in the CB and the VB. For the IR spectra, due to optical transitions in the CB, the number of allowed transitions by the

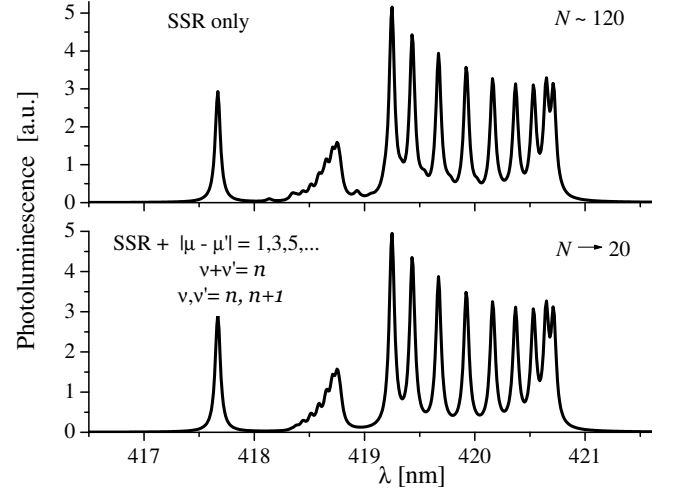


FIG. 19. PL spectra of the blue emitting InGaN system studied in the previous section. Here we plot the spectra with (lower) and without (upper) LOR. We show also the number of matrix elements that were calculated in each case.

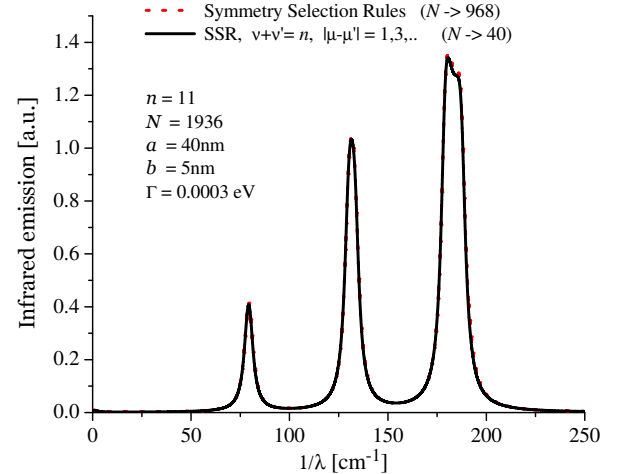


FIG. 20. Theoretical calculations of the IR spectrum with LOR (black) and without (red) for the $(GaAs/Al_x Ga_{1-x} As)^n$ SL with $x = 0.3$, valley width $a = 40\text{nm}$ and barrier width $b = 5\text{nm}$, studied in Ref. [31].

SSR when $n=11$ and $n_c=4$ is 968. However, when the LOR are taken into account, the number of evaluations reduces to $(n-1)(n_c/2)^2 = 40$. As can be seen in figure 20, there is practically no difference between the spectrum (red curve) with only SSR and the spectrum (black curve) where the SSR and LOR are taken into account. Similar results are found for PL transitions in this SL. In figure 21 we plot the PL spectra for transitions from the first four subbands in the CB to the first four *heavy hole* subbands. The transitions allowed by SSR only are plotted with a dotted curve, while those encompassing to SSR and LOR are plotted with a continuous curve.

As the third example let us now consider the $(GaAs/Al_x Ga_{1-x} As)^n$ SL studied in Ref. [30], with $x =$

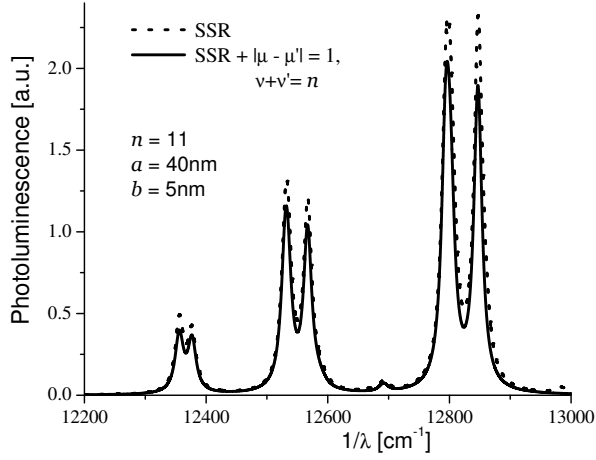


FIG. 21. Theoretical calculations of the PL spectrum with LOR (continuous) and without (dotted) for the $(GaAs/Al_xGa_{1-x}As)^n$ SL with $x = 0.3$, valley width $a = 40\text{nm}$ and barrier width $b = 5\text{nm}$, studied in Ref. [31].

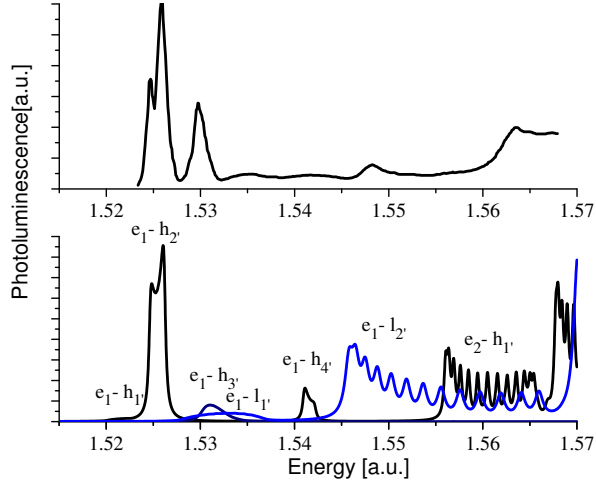


FIG. 22. PL spectra for the $(GaAs/Al_xGa_{1-x}As)^n$ SL reported in Ref. [30], with $x = 0.3$, valley width $a = 11.8\text{nm}$, barrier width $b = 1.9\text{nm}$, and conduction-band offset coefficient $Q = 0.89$. The upper panel shows the experimental results. The lower panel shows the theoretical calculation for a SL with $n=12$ and excitons in the ground state with binding energy of -5meV .

0.3 , valley width $a = 11.8\text{nm}$, barrier width $b = 1.9\text{nm}$, and conduction-band offset coefficient $Q = 0.89$. The experimental PL spectrum of this sample is shown in the upper panel of figure 22. For this system we considered an even number of unit cells, $n=12$. Thus, the allowed optical transitions occur whenever $P[\mu + \nu] \neq P[\mu' + \nu']$. To plot the PL spectrum in the lower panel of figure 22, we calculated the energy eigenvalues and eigenfunctions for all subbands, (four) in the CB, five hh -subbands and two lh -subbands in the VB, which implied the evaluation of 2,366 transition matrix elements.

The peaks of transitions $e_{1,\nu}-h_{1',\nu'}$ and $e_{1,\nu}-h_{3',\nu'}$, en-

larged in the graph, are negligible. We aligned the transitions $e_{1,\nu}-h_{2',\nu'}$ with the lowest energy peak of the experimental curve, assuming a binding energy of 5meV . To plot this PL spectrum, consider only the contributions of excitons in the ground state and $\Gamma=0.1\text{meV}$. Again we want to use this example to show that essentially the same PL spectrum can be evaluated with a much smaller number of matrix elements than those required by the SSR. Above 1.545eV the resonant structure of the optical transitions $e_{1,\nu}-l_{2',\nu'}$ and $e_{2,\nu}-h_{1',\nu'}$ shows that only a small number of transitions, of the order of the number of unit cells, contribute. For larger n or larger Γ the resonant structure becomes a continuous structure. This is what we have in figures 23 and 24, where the joint PL for the $e-hh$ and $e-lh$ transitions is plotted for $\Gamma=1\text{meV}$. In the red curve of figure 23 we have the PL that comes out when all transitions, allowed by the SSR, are taken into account, and the black curve is obtained when both the SSR and LOR are taken into account. The energy fluctuation width, in both cases, is $\Gamma=1\text{meV}$. The agreement is rather good and the reduction in the number of transition matrix elements is enormous.

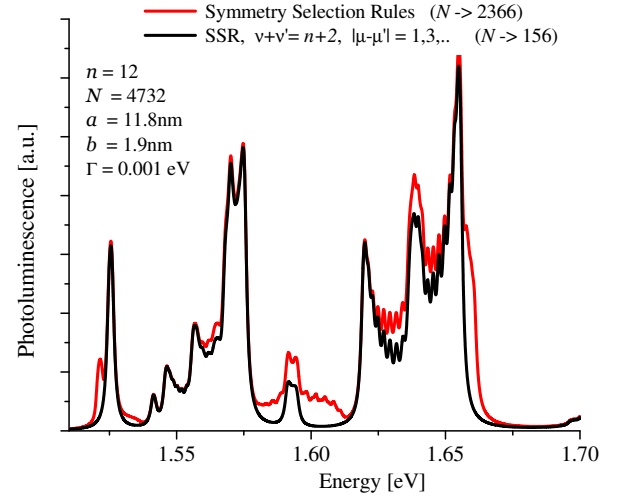


FIG. 23. The joint PL for the $e-hh$ and $e-lh$ transitions is plotted for $\Gamma=1\text{meV}$, for the $(GaAs/Al_xGa_{1-x}As)^n$ SL studied in Ref. [30], with $x = 0.3$, valley width $a = 11.8\text{nm}$, barrier width $b = 1.9\text{nm}$, and conduction-band offset coefficient $Q = 0.89$. The red curve corresponds to a PL that comes out when all transitions, allowed by the SSR, are taken into account, and the black curve is obtained when both the SSR and LOR are taken into account.

V. THE SURFACE AND EDGE STATES RULE

Just for completeness, we would like to comment briefly on a last but not less important rule, the surface and edge states rule (SESER). In the aim of simplifying the evaluation of the IR and PL spectra, we can also stress the relevance that the surface and subband-edge states have in the optical transitions. To make evident

this relevance we copy in Table 2 the matrix elements $\langle \mu', \nu' | \frac{\partial}{\partial z} | \mu, \nu \rangle$, prior to multiplication by the normalization constants, that were used to evaluate the PL spectrum of the full curve in figure 23. The darkened matrix elements, evaluated with the edge states, are the leading terms. If we are looking for the qualitative behavior of the IR or PL spectra, we can use just these matrix elements. This oversimplifying rule makes contact and coincides, only partially, with the selection rule of the standard theory. In figure 24 we plot together all the PL curves, obtained when the SSR (red), the SSR and LOR (black) and the SSR, LOR plus the surface and edge states rule (blue) are taken into account. With these examples it is clear that besides the symmetry selection rules we can use other rules according with the degree of accuracy of the experimental results or the theoretical predictions.

Finally it is worth mentioning that in our theoretical calculations, the change in the effective masses from one layer to the next has always been taken into account and the continuity conditions at the transition points were imposed always on the wave functions and their derivatives. In the last case we did not multiply by the inverse of the effective masses, as in the Ben Daniel-Duke model.¹⁰⁶ It is known³ that this can easily be done changing $k \rightarrow k/m_{ea}^*$ and $q \rightarrow q/m_{eb}^*$, etc., in the transfer matrices. The impact on the results is negligible.¹⁰⁷

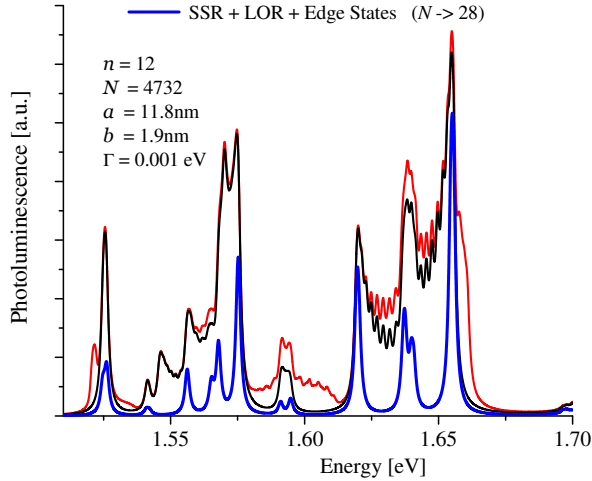


FIG. 24. Same as figure 23 but with the addition of the PL curve (blue) obtained when we take into account also the surface and edge states rule.

Table 2: Transition Matrix Elements $\langle \mu', \nu' | \frac{\partial}{\partial z} | \mu, \nu \rangle$ with $\nu + \nu' = n = 11$

μ	ν, ν'	$\mu'=2$	$\mu'=4$	$\mu'=1$	$\mu'=3$
		μ			
	1, 10	-41995.5	-5601.99	43147.6	-20794.0
	2, 9	-13935.8	-2066.66	13931.3	-7179.92
	3, 8	-8676.7	-1369.07	8463.33	-4588.9
	4, 7	-7040.9	-1151.78	6719.47	-3786.61
1	5, 6	-6731.5	-1125.58	6295.95	-3660.88
	6, 5	-7360.6	-1247.52	6755.95	-4033.15
	7, 4	-9248.4	-1580.38	8343.75	-5091.88
	8, 3	-13874.8	-2382.3	12331.1	-7659.47
	9, 2	-27581.2	-4747.98	24221.2	-15242.8
	10, 1	-102213.0	-17617.4	89060.6	-56499.7
	1, 10	22008.4	-11059.7	7468.78	12219.1
	2, 9	7218.41	-4086.48	2398.25	4139.31
	3, 8	4419.54	-2714.31	1445.49	2575.1
	4, 7	3513.77	-2291.02	1136.29	2056.49
3	5, 6	3283.2	-2246.14	1051.96	1916.54
	6, 5	3503.86	-2495.57	1112.97	2030.67
	7, 4	4296.45	-3164.7	1352.57	2464.63
	8, 3	6299.55	-4767.19	1964.46	3570.95
	9, 2	12281.3	-9481.14	3794.31	6880.33
	10, 1	44906.8	-35097.2	13773.1	24931.8

VI. CONCLUSIONS

In this paper additional applications of the theory of finite periodic systems have been presented and new selection rules for the evaluation of PL and IR spectra of optoelectronic devices, whose active region is a superlattice with an arbitrary number of unit cells, reported. We made clear the fundamental differences between the standard approach and the present theory, and consequently the differences in their prediction capabilities. We have shown that PL spectra of high accuracy experiments, that could not be explained before, are now fully understood. We have shown also that the optical transition observed experimentally, but forbidden in the standard approach, are perfectly possible within this theory. We have shown that besides the symmetry selection rules, related to the spatial symmetry of the SL eigenfunctions, one can also introduce the eigenfunctions' symmetries related with the intra-subband index, which are behind the leading order selection rules that make possible a reduction by orders of magnitude in the number of evaluations of the transition matrix elements, giving rise practically to the same PL and IR spectra. With this theory and the level of accuracy that one can reach, we not only improve the existing theory but open up the possibility of discussing other important questions related, in particular, with the parameters such as the exciton binding energies in SLs, the effective masses, the band offsets, etc., which define the optical transitions. This theory can be useful to determine more accurately their numerical values.

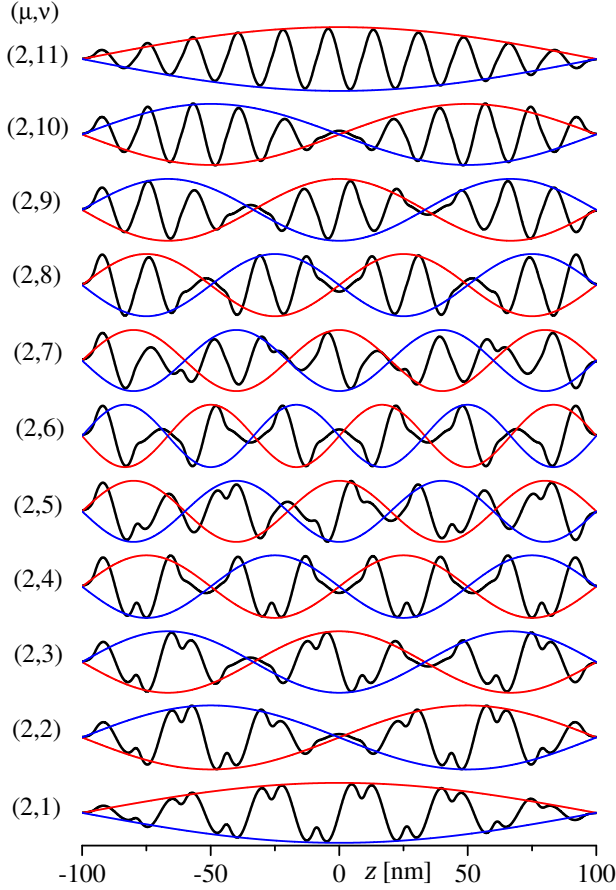


FIG. 25. Eigenfunctions in second subband of the CB. Besides the spatial symmetry with respect to the origin $z=0$, we have another symmetry with respect to the center of the subband. Thus the eigenfunctions with indices (μ, ν) and $(\mu, n+2-\nu)$ have the same symmetry. The envelopes help to visualize these symmetries.

At the end, and just for completeness, we commented on the surface and edge states selection rule, which together with the SSR and the LOR, imply the highest reduction in the number of evaluations of the transition matrix elements. The agreement with the experimental results are extremely good.

VII. ACKNOWLEDGEMENT

The author acknowledges comments and corrections of H. P. Simanjuntak, A. Robledo-Martinez and J. Grabin-sky.

Appendix A: Eigenfunction symmetries related with the intra-subband index.

In addition to the parity symmetries of the SL eigenfunctions with respect to the middle point of the superlattice, the eigenfunctions possess another symme-

try that can be recognized when we plot the whole set of intra-subband eigenfunctions. In figures 25 and 26 we plot all the eigenfunctions in the second subband of the CB and in the first subband of the VB, for the SL $(Al_{0.25}Ga_{0.75}As \setminus GaAs)^n \setminus Al_{0.25}Ga_{0.75}As$ with $a=21\text{nm}$, $b=10\text{nm}$ and $n=10$, considered in section 2 with the PL spectra of figure 15.

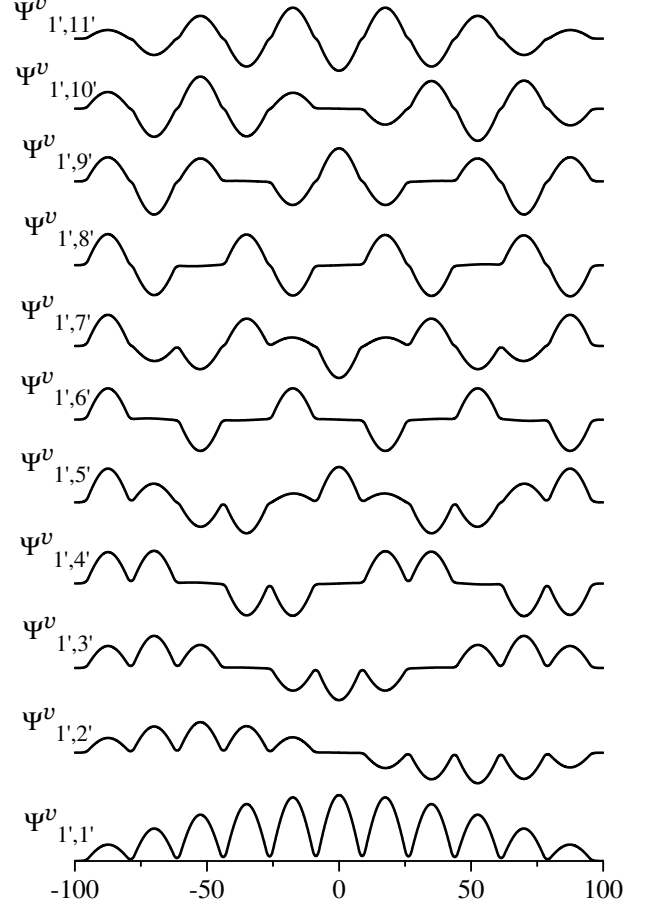


FIG. 26. Eigenfunctions in the first subband of the VB of the SL considered in figure 25. The eigenfunctions with indices (μ', ν') and $(\mu', n+2-\nu')$ have the same symmetry.

To visualize the symmetry relations between the SL eigenfunctions of the same subband, and the role of the intra-subband index ν , we plot in figure 25 guide lines (that look like envelope functions), together with the eigenfunctions $\{\Psi_{2,\nu}\}$. With the help of these guide lines we can easily recognize the symmetries that exist between pairs of intra-subband eigenfunctions. See, for example: the eigenfunctions with indices $(2, 1)$ and $(2, 11)$; the eigenfunctions with indices $(2, 2)$ and $(2, 10)$;... etc. The same happens when we plot the set of eigenfunctions of any other subband, in the conduction or valence band. In figure 26 we plot the heavy hole eigenfunctions $\{\Psi_{1',\nu'}\}$ of the first subband, with similar symmetry relations between them. In this system the surface states do not detach, therefore, as mentioned in section 3, the eigenfunctions $\Psi_{\mu,\nu}$ and $\Psi_{\mu,n+2-\nu}$ share the same sym-

metry, which is then reflected when the transition matrix elements are evaluated. As mentioned before, these symmetries are behind the matrix-elements values, thus, behind the leading order selection rules, studied in section 3.

Appendix B: The binding energy of asymmetric excitons

The calculation of the binding energy for excitons in quantum wells, double quantum wells and SLs, as well as impurities effects on the energy spectra, have been of great interest. Appropriate fitting of the optical-resonances positions led to study this problem, which is simple to visualize but rather cumbersome to obtain a rigorous solution. The actual asymmetry of the confining potential led to search variational calculations and different models of pseudo-spherical excitons. A large number of papers, based on the fractional-dimension approach, were published and binding energies of the exciton in a quantum well were obtained as functions of the well width. In these approaches the effective dimension D of the pseudo-spherical exciton lies between 2 and 3, implying binding energies between 4 and 1 Rydberg. Exciton binding energies in a SL was also addressed by Pereira et al.,⁹³ using a variational approach and a trial wave function, with similar results. For excitons in the $Al_{0.3}Ga_{0.7}As/GaAs$ SL with valley width $a=15\text{nm}$ and barrier width $b=2.5\text{nm}$ they find $E_{Bhh} \simeq 1.45E_R$ and $E_{Blh} \simeq 1.15E_R$, with E_R the effective Rydberg energy. The same year, Leavitt and Little⁹⁵ published also a simple variational method for the calculation of binding energies in quantum confined semiconductor structures. In this model the expectation energy $\langle w(\zeta) \rangle_0$ for a Hamiltonian with a Coulomb potential $1/\sqrt{u^2 + \zeta^2}$, where u and ζ are the dimensionless in-plane $\rho_e - \rho_h$ and perpendicular $z_e - z_h$ electron-hole distances, has been calculated using a trial wave function that was written in terms of a variational parameter λ , defined in such a way that correct results are obtained for both $\zeta = 0$ and $\zeta \gg u$, in the ground state $2k + 1 + m = 1$, i.e. for $k=0$ and $m=0$.

In the following subsection, we extend this model to obtain, besides the ground state expectation energy, the first excited state expectation energy $\langle w(\zeta) \rangle_1$

1. The first excited exciton state in the Leavitt-Little model

When the quasi-two-dimensional Schrödinger equation (7), is written in the center of mass and relative coordinates, the radial part, for the azimuthal quantum number $m=0$, is

$$\left[\frac{\hbar^2}{2\mu_{||}} \frac{1}{\rho} \frac{d}{d\rho} \rho \frac{d}{d\rho} - \frac{e^2}{\epsilon \sqrt{\rho^2 + z^2}} \right] g_\eta(\rho, z) = E_\eta^{(2D)} g_\eta(\rho, z) \quad (B1)$$

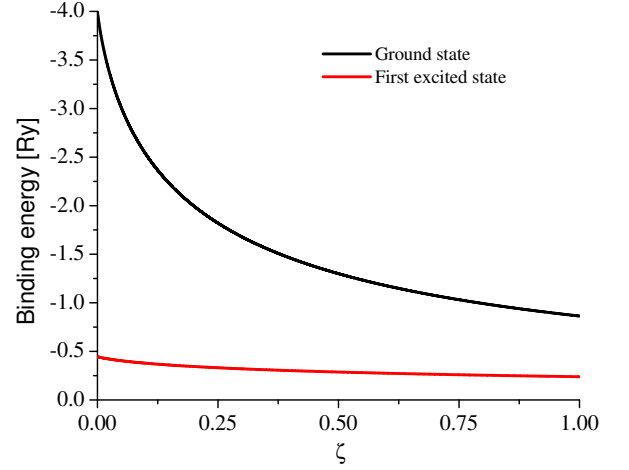


FIG. 27. The expected exciton binding energies $\langle w \rangle_0$ (upper curve) and $\langle w \rangle_1$ as FUNCTIONS of ζ . The difference between the ground and the first excited state, measured in units of R_y , reduces as the exciton dimension grows from $D=2$ to $D=3$.

where $z=z_e-z_h$ and $\mu_{||}$ the in-plane relative $e-h$ effective mass. Defining $u=\rho/a_0$, $\zeta=(z_e-z_h)/a_0$, $w_\eta(\zeta)=E^{(2D)}_\eta/E_0$ and $G_\eta(u;\zeta)=a_0 g_\eta(u;\zeta)$, where $a_0=\epsilon\hbar^2/\mu_{||}e^2$ and $E_0=\mu_{||}e^4/2\epsilon^2\hbar^2$, we have the dimensionless differential equation

$$\left(\frac{1}{u} \frac{d}{du} u \frac{d}{du} - \frac{2}{\sqrt{u^2 + \zeta^2}} \right) G_\eta(u, \zeta) = w_\eta(\zeta) g_\eta(u, \zeta). \quad (B2)$$

Knowing the exact solutions: $G_0(u;0) = (1/u)e^{-2u}$ with $w_0(0) = 4$, for $\zeta = 0$, and $G_0(u;\zeta \gg 1) = \sqrt{2}e^{-u^2/2\zeta^{3/2}}/u\zeta^3$ with $w_0(\zeta) = 2/\zeta - 2/\zeta^{3/2}$, for $\zeta \gg u$, the trial function

$$G_0(u, \zeta) = N e^{-\lambda_0(\sqrt{u^2 + \zeta^2} - \zeta)} \quad (B3)$$

has been suggested, with N a normalization constant and λ_0 a variational parameter chosen as $\lambda_0 = 2/(1 + 2\sqrt{\zeta})$, in such a way that as $\zeta \rightarrow 0$ ($\lambda_0 \rightarrow 2$), and for $\zeta \gg 1$ ($\lambda_0 \rightarrow 1/\sqrt{\zeta}$), the trial wave function approaches the correct results. Since the first excited energy and the exact solutions are also known in these limits: $w_k = 4/(2k + 1 + 2m)^2$ for $\zeta = 0$ and $w_k = 2/\zeta(1 - (2k + 1 + m)/\sqrt{\zeta})$ for $\zeta \gg u$, we propose the trial wave function

$$G_k(u, \zeta) = N e^{-\lambda_k(\sqrt{u^2 + \zeta^2} - \zeta)} [1 - 2\lambda_k(\sqrt{u^2 + \zeta^2} - \zeta)]^k \quad (B4)$$

with

$$\lambda_k = \frac{2}{2k + 1 + m + 2\sqrt{\zeta}}. \quad (B5)$$

The expectation values of the binding energy

$$\langle w_k(\zeta) \rangle = \frac{\int_0^\infty G_k^*(u, \zeta) \hat{H}_{2D} G_k(u, \zeta) u du}{\int_0^\infty |G_k(u, \zeta)|^2 u du}, \quad (B6)$$

become, for $k = 0$ and $k = 1$, respectively,

$$\langle w_0(\zeta) \rangle = -\lambda_0^2 + \frac{4\lambda_0 + 4\zeta^2\lambda_0^4}{1 + 2\sqrt{\zeta}} e^{2\zeta\lambda_0} \Gamma(0, 2\zeta\lambda_0), \quad (\text{B7})$$

and

$$\langle w_1(\zeta) \rangle = -4e^{2\zeta\lambda_1} \zeta^2 \lambda_1^4 (3 + 2\zeta\lambda_1) \Gamma(0, 2\zeta\lambda_1)$$

$$+ \frac{4\lambda_1 - \lambda_1^2(3 + 2\zeta\lambda_1(5 + 2\zeta\lambda_1(5 + 2\zeta\lambda_1)))}{3 + 2\zeta\lambda_1}.$$

In figure A1 we plot the expectation value of the hh -exciton binding energies in the ground and first excited states. The ratio between these energies changes from a factor of 9 in the 2D limit to a factor that tends to 1 for large ζ .

-
- ¹ Y. B. Band, *Light and Matter: electromagnetism, optics, spectroscopic and lasers*, John Wiley & Sons Ltd. (2006), and references therein.
- ² F. Bloch, *Z. Physik* **52** 555 (1928).
- ³ G. Bastard, *Wave Mechanics Applied to Semiconductor Heterostructures*, (Les Editions de Physique, Les Ulis Cedex, France 1988)
- ⁴ P. Pereyra, *Ann. Phys.* **320**, 1 (2005).
- ⁵ M. Altarelli in *Heterojunctions and Semiconductor Superlattices: Proceedings of the Winter School Les Houches* Ed. by Guy Allan and Gerald Bastard, France, March 12-21, 1985. Altarelli noticed, in this reference, that the effective mass approximation has proven to be simple, accurate and versatile for the calculation of electronic levels, and superior to other methods with the remarkable feature that all references to the microscopic structure of the host semiconductor is condensed in the effective mass m^* and the band edge $E_n(0)$.
- ⁶ Pereyra P. arXiv condmatt 1607.02685.
- ⁷ L. V. Keldysh *Fiz. Tverd. Tela* **4**, 2265 (1962), English translation, in *Sov. Phys. -Solid State* **4**, 1658 (1963).
- ⁸ L. Esaki and R. Tsu, *IBM J. Res. Develop.* **14**, 61 (1970); Esaki 1972
- ⁹ L. L. Chang, L. Esaki, R. Tsu, *Appl. Phys. Lett.* **24**, 593 (1974).
- ¹⁰ R. Dingle, W. Wiegmann and C. H. Henry *Phys. Rev. Lett.* **33**, 827 (1974).
- ¹¹ Mukherji, *Phys. Rev. B* **12**, 4338 (1975).
- ¹² R. C. Miller, R. Dingle, A. C. Gossard, R. A. Logan, W. A. Nordland Jr. and W. Wiegmann, *J. Appl. Phys.* **47**, 4509 (1976).
- ¹³ L. L. Chang, H. Sakaki, C. -A. Chang and L. Esaki, *Phys. Rev. Lett.* **45**, 1489 (1977).
- ¹⁴ G. A. Sai-Halasz, L.L. Chang, J. -M. Welter, C. -A. Chang and L. Esaki *Sol. Stat. Comm.* **27**, 935 (1978).
- ¹⁵ D. A. B. Miller, D. S. Chemla, D. J. Eilenberger, P. W. Smith, A. C. Gossard and W. T. Tsang, *Appl. Phys. Lett.* **41**, 679 (1982).
- ¹⁶ G. Belle, J. C. Maan and G. Weimann, *Sol. Stat. Comm.* **56**, 65 (1985).
- ¹⁷ F. Capasso, K. Mohammed and A. Y. Cho, *IEEE J. Quantum Elect.* **QE22**, 1853 (1986).
- ¹⁸ P. England, J. R. Hates, E. Colas and M. Helm, *Phys. Rev. Lett.* **63**, 1708 (1989).
- ¹⁹ H. Luo and J. K. Furdyna, *Phys. Rev. B* **41**, 55188 (1990).
- ²⁰ J. H. Luscombe, R. Aggarwal, M. A. Reed, W. R. Fremley and M. Luban, *Phys. Rev. B* **44**, 5873 (1991).
- ²¹ C. Rauch, G. Strasser, K. Unterrainer, E. Gornik and B. Brill, *Appl. Phys. Lett.* **70**, 679 (1997).
- ²² G. Scamarcio, F. Capasso, J. Faist, C. Sirtori, D. L. Sivco, A. Hutchinson and A. Y. Cho *Appl. Phys. Lett.* **70**, 1796 (1997).
- ²³ M. V. Petrov and S. Lyon, *Appl. Phys. Lett.* **70**, 3269 (1997).
- ²⁴ R. Heer, J. Smoliner, G. Strasser and E. Gornik, *Appl. Phys. Lett.* **73**, 3138 (1998).
- ²⁵ R. Dingle, A. C. Gossard and W. Wiegmann, *Phys. Rev. Lett.* **34**, 1327 (1975).
- ²⁶ R. Tsu A. Koma and L. Esaki, *J. Appl. Phys.* **46**, 842 (1975).
- ²⁷ A. Chomette, B. Deveaud, M. Baudet, P. Auvray and A. Regreny, *J. Appl. Phys.* **59**, 3835 (1986).
- ²⁸ P. F. Yuh and K. L. Wang, *Appl. Phys. Lett.* **51**, 1404 (1987).
- ²⁹ Y. Fu and K. A. Chao, *Phys. Rev. B* **40**, 8349 (1989).
- ³⁰ M. Helm, F. M. Peeters, F. DeRosa, E. Colas, J. P. Harbison and L. T. Florez, *Phys. Rev. B* **43**, 13983 (1991).
- ³¹ Y. Fu, M. Willander and W. Xu, *J. Appl. Phys.*, **77**, 4648 (1995).
- ³² S. Glutsch, D. S. Chemla and F. Bechstedt *Phys. Rev. B* **54**, 11592 (1996).
- ³³ H. Haug and A-P. Jauho *Quantum Kinetics in Transport an Optics in Semiconductors* (Springer, Heidelberg, 2008 2nd Ed.)
- ³⁴ K. Leo, *Semicond. Sci. Technol* **13**, 249 (1998).
- ³⁵ L. Esaki, in *Heterojunctions and Semiconductor Superlattices: Proceedings of the Winter School Les Houches* Ed. by Guy Allan and Gerald Bastard, France, March 12-21, 1985.
- ³⁶ Yia Chung Chang and J. N. Schulman, *Appl. Phys. Lett.* **43**, 536 (1983).
- ³⁷ M. M. Dignam and J. E. Sipe, *Phys. Rev. B* **41**, 2865 (1990).
- ³⁸ J. C. Slater, *Phys. Rev.* **76**, 452 (1949).
- ³⁹ H. M. James, *Phys. Rev.* **76**, 1611 (1949).
- ⁴⁰ G. T. Einevoll and P. C. Hemmer, *J. Phys. C: Solid State Phys.* **21**, L1193 (1988)
- ⁴¹ G. Bastard, *Phys. Rev. B* **24**, 5693 (1981). G. Bastard, *Phys. Rev. B* **25**, 7584 (1982).
- ⁴² S. R. White and L. J. Sham, *Phys. Rev. Lett.* **47**, 879 (1981).
- ⁴³ C. Mailhot, Yia-Chung Chang and T. C. McGill, *Phys. Rev. B* **26**, 4449 (1982)
- ⁴⁴ L. W. Molenkamp, G. E. W. Bauer, R. Eppenga and C. T. Foxon, *Phys. Rev. B* **38**, 6147 (1988).
- ⁴⁵ M. Helm, W. Hilbert, T. Fromherz, F. M. Peeters, K. Alavi and R. N. Pathak, *Phys. Rev. B* **48**, 1601 (1993).
- ⁴⁶ M. Virgilio, M. Bonfanti, D. Chrastina, A. Neels, G. Isella, E. Grilli, M. Guzzi, G. Grosso, H. Sigg and H. von Känel, *Phys. Rev. B* **79**, 075323 (2009).
- ⁴⁷ R. Dingle, *Festkörper Probleme XV, Advances in Solid State Physics*, (Ed. H. J. Queisser, Pergamon and Vieweg

- & Sohn, Stuttgart 1975).
- ⁴⁹ G. D. Sanders and Yia-Chung Chang, *Phys. Rev. B* **32**, 5517 (1985).
 - ⁵⁰ W. T. Masselink, P. J. Pearah, J. Klem, C. K. Peng, H. Morkoc, G. D. Sanders and Yia-Chung Chang, *Phys. Rev. B* **32**, 8027 (1985).
 - ⁵¹ D. C. Reynolds, K. K. Bajaj, C. Leak, G. Peters, W. Theis, P. W. Yu, K. Alavi, C. Colvard and I. Shidlovsky *Phys. Rev. B* **37**, 3117 (1988).
 - ⁵² Y. Fu and K. A. Chao, *Phys. Rev. B* **40**, 8349 (1989).
 - ⁵³ W. Zhu, Q. Shen and S. Liu, *J. Phys: Condens. Matter* **7**, 9693 (1995).
 - ⁵⁴ See page 247 of S. Nakamura, S. Pearton and G. Fasol, *The Blue Laser Diode. The complete history* (Springer-Verlag, Berlin Heidelberg 1997)
 - ⁵⁵ S. Nakamura, M. Senoh, S. Nagahama, N. Iwasa, T. Yamada, T. Matsushita, H. Kiyoku and Y. Sugimoto, *Jpn. J. Appl. Phys.* **35**, L217 (1996), *Appl. Phys. Lett.* **68**, 3269 (1996).
 - ⁵⁶ Y. Nawakami, S. Fujita, S. Fujita and S. Nakamura, *Phys. Rev. B* **55**, R1938 (1997).
 - ⁵⁷ Y. Narukawa, Y. Kawakami, S. Fujita and S. Nakamura, *Phys. Rev. B* **59**, 10283 (1999).
 - ⁵⁸ G. A. SaiHalasz, R. Tsu and L. Esaki, *Sol. Stat. Comm.* **27**, 935 (1978).
 - ⁵⁹ G. Yang, S. Lee and J. K. Furdyna, *Phys. Rev. B* **61**, 10978 (2000).
 - ⁶⁰ H. Haug and S. W. Koch Quantum Theory of the optical and Electronic Properties of Semiconductors (4th. Ed. World Scientific, Singapore 2004).
 - ⁶¹ It is clear that theoretical approaches designed to deal with subbands, are not able to distinguish intra-subband optical transitions from each other, and the intra-subband effects will be beyond their prediction ability. To correct this deficiency, it was necessary, in the tight-binding model,^{11,19,37,46,47} to include specific atomic states in the superlattice, in order to understand and to account for the optical response at low frequencies.
 - ⁶² R. Landauer, *Philos. Mag.* **21**, 863 (1970).
 - ⁶³ F. Abeles, *Ann. Phys. (Paris)* **5**, 596 (1950); **5**, 706 (1950).
 - ⁶⁴ M. Born and E. Wolf, *Principles of Optics* (Dover, Pergamon, Oxford, 1980)
 - ⁶⁵ R. de L. Kronig and W. G. Penney, *Proc. Roy. Soc. (London)* **A130**, 499 (1931).
 - ⁶⁶ Tsu and Esaki, computed resonant transmission coefficients of double, triple and quintuple barrier structures, based on explicit solutions of the Schrödinger-equation for sectionally-constant 1D potentials, and using transfer matrices.
 - ⁶⁷ P. Erdös and R. C. Herndon, *Adv. Phys.* **31**, 65 (1982).
 - ⁶⁸ M. Pacheco and F. Claro, *Phys: Status Solidi B* **114**, 399 (1982).
 - ⁶⁹ B. Ricco and M. Ya. Azbel, *Phys. Rev. B* **29**, 1970 (1984).
 - ⁷⁰ D. J. Vezzetti and M. Cahay, *J. Phys. D* **19**, L5355 (1986).
 - ⁷¹ R. Pérez-Alvarez and H. Rodríguez-Coppola, *Phys. Status Solidi (b)* **145**, 493 (1988).
 - ⁷² H. W. Lee, A. Zysnarsky, and P. Kerr, *Am. J. Phys.* **57**, 729 (1989).
 - ⁷³ H. Cruz, A. Hernández-Cabrera and P. Aceituno, *J. Phys.: Condens. Matter* **2**, 8953 (1990).
 - ⁷⁴ T. H. Kolatas and A. R. Lee, *Eur. J. Phys.* **12**, 275 (1991).
 - ⁷⁵ D. J. Griffiths and N. F. Taussing, *Am. J. Phys.* **60**, 883 (1992).
 - ⁷⁶ D. W. Sprung, H. Wu, and J. Martorell, *Am. J. Phys.* **61**, 1118 (1993).
 - ⁷⁷ M. G. Rozman, P. Reineker, and R. Tehver, *Phys. Lett. A* **187**, 127 (1994).
 - ⁷⁸ Yu. G. Peisakhovich, *J. Phys. A*, **29**, 5103 (1996)
 - ⁷⁹ P. Pereyra, *Phys. Rev. Lett.* **80** (1998) 2677; P. Pereyra, *J. Phys. A* **31**, 4521 (1998).
 - ⁸⁰ P. Yeh, *Optical Waves in Layered Medias*, John Wiley & Sons, New York (1998).
 - ⁸¹ P. Pereyra, *Phys. Rev. Lett.* **84**, 1772 (2000); J. L. Cardoso, P. Pereyra and A. Anzaldo-Meneses, *Phys. Rev. B* **63**, 153301 (2001).
 - ⁸² P. Pereyra, arXiv:cond-mat/0009064v1 [con-mat.soft] 5 Sep 2000.
 - ⁸³ P. Pereyra and E. Castillo, *Phys. Rev. B* **65**, 205120 (2002).
 - ⁸⁴ F. Assaoui and P. Pereyra, *J. Appl. Phys.* **91**, 5163 (2002); M. F. Avila-Ortega and P. Pereyra, *Superlattices and Microstructures* **43**, 645 (2008).
 - ⁸⁵ A. Kunold and P. Pereyra, *J. App. Phys.* **93**, 05018 (2003).
 - ⁸⁶ C. Pacher and E. Gornik, *Phys. Rev. B* **68**, 155319 (2003).
 - ⁸⁷ H. P. Simanjuntak and P. Pereyra, *Phys. Rev. B* **67**, 045301 (2003). P. Pereyra and H. P. Simanjuntak, *Phys. Rev. E* **75**, 056604 (2007).
 - ⁸⁸ P. Pereyra, *Fundamentals of Quantum Physics* (Springer-Verlag, Berlin Heidelberg 2012)
 - ⁸⁹ F. Avila-Ortega and P. Pereyra, *Superlattices and Microstructures* **43**, 645 (2008); P. Pereyra and F. Avila-Ortega, *Superlattices and Microstructures* **52**, 24 (2012).
 - ⁹⁰ We consider these Hamiltonians in the effective mass approximation, which as Altarelli⁵ states, has proven to be simple, accurate and versatile for the calculation of electronic levels, and superior to other methods with the remarkable feature that all reference to the microscopic structure of the host semiconductor is condensed in the effective mass m^* and the band edge $E_n(0)$.
 - ⁹¹ R. L. Greene, K. K. Bajaj and D. W. Phelps, *Phys. Rev. B* **29**, 1807 (1984).
 - ⁹² A. Chomette, B. Lambert, B. Deveaud, F. Clerot, A. Regreny and G. Bastard, *Europhys. Lett.* **4**, 461 (1987).
 - ⁹³ M. F. Pereira Jr. I. Galbraith, S. W. Koch and G. Duggan, *Phys. Rev. B* **41**, 7084 (1990).
 - ⁹⁴ L. C. Andreani and A. Pasquarello, *Phys. Rev. B* **42**, 8928 (1990).
 - ⁹⁵ R. P. Leavitt and J. W. Little, *Phys. Rev. B* **42**, 11774 (1990).
 - ⁹⁶ P. Christol, P. Lefebvre and H. Mathieu, *J. Appl. Phys.* **74**, 5626 (1993).
 - ⁹⁷ A. Matos-Abiague, L. E. Oliveira and M. De Dios-Leyva, *Phys. Rev. B* **58**, 4072 (1998).
 - ⁹⁸ See page 247 in Ref. [54].
 - ⁹⁹ It is known that in the zincblende structure $E_{g,GaN} = 3.2\text{eV}$, while in the wurtzite structure $E_{g,GaN} = 3.4\text{eV}$. A difference of 0.2eV could not be explained taking into account the charge polarization effect. This effect, as was shown in Fatna an Kunold, might produce a shift in the subband positions of the order of 40meV, as much.
 - ¹⁰⁰ M. Helm, W. Hilber, T. Fromhertz, F. M. Peeters, K. Aalavi and R. N. Pathak, *Solid-State Electronics* **37**, 1277 (1994).
 - ¹⁰¹ M. Helm, *Semicond. Sci. Technol.* **10**, 557 (1995).
 - ¹⁰² See page 267 in Ref. [54] .
 - ¹⁰³ P. W. Yu et al. *Phys. Rev. B* **35**, 9250 (1987).

- ¹⁰⁴ The reductions depend on whether the number of subbands n_c are even or odd. If $\nu + \nu' = n$ the reduction is from $(n+1)^2 n_c^2/2$ to $(n-1)(n_c/2)^2$ for n_c even and $(n-1)n_c(n_c+1)/2$ for n_c odd. When $\nu + \nu' = n+2$ the reduction is from $(n+1)^2 n_c^2/2$ to $(n+1)(n_c/2)^2$ for n_c even and $(n+1)n_c(n_c+1)/2$ for n_c odd.
- ¹⁰⁵ Parameters published by the Ioffe Physico-Technical Institute, St. Petersburg, Russian Federation.
- ¹⁰⁶ D. J. BenDaniel and C. B. Duke, *Phys. Rev.* **152**, 683 (1966).

- ¹⁰⁷ The differences in the band structure taking into account a) the continuity of the wave functions and their derivatives and the continuity of the wave functions and their derivatives multiplied by the inverse of the effective masses, the so-called Ben Daniel-Duke continuity conditions, is in the low energy subbands of the order of 0.1meV while in the higher energy subbands of the order of 1meV, as was shown by Bastard³